

Photometric classification of supernovae detected by the Zwicky Transient Facility using noise augmentation

A. Townsend^{1, *} , J. Nordin¹ , M. Kowalski^{1, 2} , S. Reusch³ , J. P. Anderson⁴ , E. C. Bellm⁵ , U. Burgaz⁶ , T. X. Chen⁷ , T.-W. Chen⁸ , G. Dimitriadis⁹ , L. Galbany^{10, 11} , A. Goobar¹² , M. J. Graham¹³ , M. Gromadzki¹⁴ , C. P. Gutiérrez^{10, 11} , D. Hale¹⁵ , C. Inserra¹⁶ , M. M. Kasliwal¹³ , Y.-L. Kim¹⁷ , K. Maguire⁶ , F. J. Masci⁷ , T. E. Müller-Bravo^{6, 18} , D. A. Perley¹⁹ , R. L. Riddle⁷ , M. Rigault²⁰ , J. van Santen² , S. Schulze²¹ , M. Smith⁹ , J. Sollerman²² , and S. Yang²³ 

(Affiliations can be found after the references)

Received; accepted

ABSTRACT

Context. Modern time-domain surveys, such as the Zwicky Transient Facility (ZTF), detect far more extragalactic transients than can be spectroscopically classified. Photometric classification offers a scalable alternative, enabling the identification of larger, fainter, and higher-redshift supernova samples suitable for applications such as Type Ia supernova (SN Ia) cosmology.

Aims. We present a feature-based photometric classifier for SNe detected by ZTF, with the primary goal of constructing a photometric SN Ia sample for cosmological analyses.

Methods. Our approach utilises the autoencoder architecture from the ParSNIP model (Boone 2021) to capture the intrinsic diversity of SN light curves. We trained the model on a spectroscopically classified ZTF SN sample, incorporating a realistic noise augmentation procedure that simulates the flux uncertainties of fainter sources. This enables the model to generalise to noisier, higher-redshift populations. Light curve features were used to train a gradient-boosted decision tree classifier, implemented in both binary (SN Ia vs. non-Ia) and multi-class configurations. We validated our classifier on independent, fainter ZTF data with and without noise augmentation. To evaluate real-time performance, we also applied our classifier to live ZTF alerts and conducted a spectroscopic classification survey within the ePESSTO+ collaboration.

Results. We found that noise augmentation significantly improves classification performance, particularly for fainter sources. Our binary classifier achieves an SN Ia recall of $(98.1 \pm 0.4)\%$, averaged across five train–test splits. SN Ia recall exceeds 98% for events with a peak apparent magnitude up to 20 and more than 10 detections, and remains above 96% up to magnitude 20.5. Overall, 95% of sources were correctly classified in both binary and multi-class modes. In our live classification survey, we correctly identified the class for 78% of the targets, including rare events such as superluminous supernovae, despite a median of only nine detections per object.

Conclusions. Our classifier performs efficiently on real ZTF data, including faint and noisy light curves. Applied to the full ZTF transient sample, it will enable construction of a large photometric SN Ia dataset for cosmology. It also provides a practical tool for real-time spectroscopic target prioritisation, which will be essential for large-scale surveys such as the Vera C. Rubin Observatory’s Legacy Survey of Space and Time.

Key words. supernovae: general – Methods: data analysis

1. Introduction

In the era of wide-field, time-domain surveys such as the Zwicky Transient Facility (ZTF; Bellm et al. 2019b; Graham et al. 2019), significantly more extragalactic transients are detected than can be spectroscopically classified with available resources. The volume of data is expected to increase dramatically with the arrival of deeper and more sensitive surveys, such as the Vera C. Rubin Observatory’s Legacy Survey of Space and Time (LSST; Ivezić et al. 2019). This has driven the development of accurate, scalable, and robust machine learning classifiers capable of identifying and classifying transients using photometric data alone, with minimal reliance on spectroscopic follow-up.

A variety of classification approaches have emerged, ranging from feature-based methods (e.g., Lochner et al. 2016; Villar et al. 2019; Boone 2019; Miranda et al. 2022; de Soto et al. 2024) and template-fitting methods (e.g., Sako et al. 2011) to deep learning architectures (e.g., Muthukrishna et al. 2019; Möller & de Boissière 2020; Boone 2021; Qu et al. 2021; Pimentel et al. 2023), semi-supervised learning (e.g., Richards et al. 2012; Vil-

lar et al. 2020), transfer learning (e.g., Zhang et al. 2024a), and active learning (e.g., Kennamer et al. 2020; Leoni et al. 2022). Some classifiers are specialised to find rare transients such as superluminous supernovae (SLSNe) or tidal disruption events (TDEs) (e.g., Gomez et al. 2020; Sheng et al. 2024; Stein et al. 2024). While most classifiers rely exclusively on the photometric data of the transient itself, some have been developed that use only information from the host galaxy (e.g., Gagliano et al. 2021; Kisley et al. 2023).

Real-time brokers and pipelines such as the Automatic Learning for the Rapid Classification of Events Alert Broker (ALeRCE; Förster et al. 2021) and Fink (Leoni et al. 2022) have demonstrated the practical utility of these models in live survey operations. Several additional classifiers have been developed to enable rapid detection and classification of transients in real-time surveys, using limited early-time photometric data. (e.g., Muthukrishna et al. 2019; Miranda et al. 2022; Gagliano et al. 2023; Zhang et al. 2024b). Furthermore, classification challenges that simulate live surveys continue to encourage innovation in the community, such as the Supernova Photometric Classification Challenge (SPCC, Kessler et al. 2010) and the

* Corresponding author; alice.townsend@physik.hu-berlin.de

LSST data challenges with PLAsTiCC and ELAsTiCC simulations (Hložek et al. 2023; Narayan & ELAsTiCC Team 2023; Shah et al. 2025; Nordin et al. 2025).

One persistent issue in the field is the small and biased sample of spectroscopically confirmed supernovae available for model training. It is well established that machine learning models trained on samples that are not representative of the test sample tend to perform poorly. This limitation was highlighted in the SPCC (Kessler et al. 2010; Richards et al. 2012; Lochner et al. 2016), where the simulated training set was intentionally biased toward bright, low-redshift events typical of spectroscopic follow-up campaigns. Some classifiers addressed this challenge by augmenting the training set using Gaussian Process (GP; Rasmussen & Williams 2006) models fitted to the original light curves. These GP-based methods generate additional synthetic light curves to better populate underrepresented regions of feature space, improving classification performance on the simulated test sets (Revsbech et al. 2018; Pasquet et al. 2019; Boone 2019). Pasquet et al. (2019) and Boone (2019) also introduced additional forms of noise augmentation, either by adding noise to the flux values or by resampling the redshift and scaling the flux accordingly. Both studies included further augmentation strategies such as randomly dropping observations or applying random time shifts. Further analyses using simulated LSST data have reinforced the effectiveness of this augmentation approach (Carrick et al. 2021; Alves et al. 2022). Although these results are promising, so far they are only validated on simulated datasets. Studies have shown that a model solely trained on simulated data performs poorly when classifying real data (e.g., Revsbech et al. 2018).

In a different approach, Boone (2021) proposed to solve the issue of non-representative datasets with ParSNIP¹, a deep learning model designed to be invariant to observing conditions and to the transient distance. The model learns a latent representation of each light curve by explicitly disentangling the intrinsic features of the transient (such as its brightness evolution and colour) from observational factors such as redshift, host galaxy extinction, and survey cadence. This allows the model to generalise more effectively across the biased datasets typical of real surveys. ParSNIP has previously been utilised to classify a photometric SN sample for the Young Supernova Experiment Data Release 1 (YSE DR1; Aleo et al. 2023) and to make predictions for photometric classification using simulated Roman Space Telescope data (Abdelhadi & Rubin 2024).

Currently, the majority of photometric classifiers are trained and tested on simulated datasets to compensate for the lack of real, labelled data. However, these simulations, which are generated from transient template models, often fail to capture the full diversity of real transients. In this work, we extend the previous studies on noise augmentation by applying a new methodology to real data from ZTF. We have combined the ParSNIP model of Boone (2021) with our noise augmentation algorithm to demonstrate that we can accurately classify the noisier and more sparsely sampled candidate supernovae found in the ZTF archive.

1.1. The application of photometric classifiers in supernova cosmology

Type Ia supernovae (SNe Ia) are precise cosmological distance indicators due to their nearly uniform peak luminosities, enabling their use as standardisable candles (e.g., Phillips 1993;

Riess et al. 1996; Tripp 1998). This approach led to the discovery of the accelerating expansion of the universe, attributed to dark energy (Riess et al. 1998; Perlmutter et al. 1999). Today, SNe Ia remain essential for constraining key cosmological parameters such as the Hubble constant (H_0) and the dark energy equation-of-state parameter (w).

Since the discovery of cosmic acceleration, based on a sample of approximately 40 SNe Ia, progressively larger datasets have been employed in cosmological analyses. One of the most comprehensive of these is the Pantheon+ compilation, which includes 1550 spectroscopically confirmed SNe Ia (Brout et al. 2022). The ZTF SN Ia data release 2 (DR2; Rigault et al. 2025) provides a publicly available sample of 3628 spectroscopically classified SNe Ia, which is the largest release of SNe Ia to date and increases the sample of low redshift SNe Ia by an order of magnitude. In recent years, analyses with samples of photometrically classified SNe Ia – such as those from Pan-STARRS (PS1; Jones et al. 2018), the Sloan Digital Sky Survey (SDSS; Sako et al. 2011; Campbell et al. 2013) and combined datasets (Popovic et al. 2024) – have demonstrated that unbiased cosmological parameters can be recovered, in agreement with those derived from spectroscopically confirmed samples.

A notable example is the Dark Energy Survey (DES; Abbott et al. 2019; DES Collaboration et al. 2024), which recently released cosmological constraints based on a sample of 1635 photometrically identified SNe Ia (Möller et al. 2022; Vincenzi et al. 2024). DES used SuperNNova (Möller & de Boissière 2020) as the baseline photometric classifier, supplemented with cross-checks using alternative methods such as SCONE (Qu et al. 2021). Simulations suggest a classification accuracy and purity exceeding 98% (Vincenzi et al. 2021, 2023). Crucially, the impact of photometric misclassification was found to be small, with uncertainties from photometric classification contributing less than 10% of the total systematic error budget.

To incorporate classification uncertainties into the cosmological analysis, both DES and PS1 adopted probabilistic frameworks. These analyses used the Bayesian Estimation Applied to Multiple Species (BEAMS; Kunz et al. 2013; Hložek et al. 2012) approach or its extension, BEAMS with Bias Corrections (BBC; Kessler & Scolnic 2017). BEAMS marginalises over the probability that each event is an SN Ia, thereby accounting for contamination from core-collapse SNe. The BBC extension applies corrections to the observed distance moduli, accounting for selection effects, contamination, and light curve fitting biases, all derived from realistic simulations. This enables the construction of a bias-corrected Hubble diagram from photometrically classified SNe Ia.

The results of these studies indicate that contamination from other SN types in photometrically classified samples can be limited to approximately 5% (e.g., Jones et al. 2018; Vincenzi et al. 2021, 2023; Möller et al. 2022). At this level, contamination is a subdominant source of uncertainty, and cosmological constraints remain comparable to those from spectroscopic samples if classification probabilities and selection effects are correctly modelled. As a result, improving SN Ia classification completeness (also known as recall) is key to increasing the statistical power of photometric samples. In the following analysis, we focus on SN Ia recall as the primary classifier performance metric.

In this work, we present a feature-based photometric classifier for SNe detected by ZTF, with the primary goal of constructing a photometric SN Ia sample for cosmological analyses. Our approach utilises the autoencoder architecture from the ParSNIP model (Boone 2021) to capture the intrinsic diversity of SN light curves. We trained the model on a spectroscopically clas-

¹ github.com/LSSTDESC/parsnip

sified ZTF SN sample, incorporating a realistic noise augmentation procedure that simulates the flux uncertainties of fainter sources. This enables the model to generalise to noisier, higher-redshift populations. Light curve features were used to train a gradient-boosted decision tree classifier, implemented in both binary (SN Ia vs. non-Ia) and multi-class configurations. We validated our classifier on independent, fainter ZTF data with and without noise augmentation. To evaluate real-time performance, we also applied our classifier to live ZTF alerts and conducted a spectroscopic classification survey within the extended Public ESO Spectroscopic Survey for Transient Objects (ePESSTO+; Smartt et al. 2015) at the 3.5-metre ESO New Technology Telescope (NTT).

The structure of this paper is as follows. Section 2 summarises the ZTF data used in this analysis, the transient classes considered, and how we divided the training and test samples. In Sect. 3, we describe how we modelled the ZTF flux uncertainties to simulate higher-redshift sources and detail the noise augmentation procedure used to improve classification performance. Section 4 outlines the generation of training and test sets, the training of the ParSNIP model, and the creation of the classifiers. In Sect. 5, we present the classification results, discuss the optimisation of the augmentation parameters, and highlight the performance of one of our best models. We further evaluate the classifier on additional datasets, including the ZTF SN Ia DR2 sample (Sect. 5.3) and peculiar or uncommon subtypes initially excluded (Sect. 5.4). We then discuss applications of our method to SN Ia cosmology (Sect. 5.5) and real-time transient classification (Sect. 5.6), which includes results from a live classification survey conducted with the ePESSTO+ collaboration. Finally, Sect. 6 summarises our key findings and outlines the future steps toward constructing a photometrically classified ZTF SN sample.

2. Data

ZTF is an optical, wide-field, survey designed for time-domain astronomy (Bellm et al. 2019b; Graham et al. 2019). It operates using a 47-square-degree field-of-view camera mounted on the 48-inch telescope at Palomar Observatory (P48), which observes in three photometric bands: g , r and i (Dekany et al. 2020). The observing strategy includes a publicly available survey in g - and r -bands that surveys the northern sky every two days, alongside a higher-cadence partnership survey that includes i -band observations over a more limited area. The public survey initially operated on a three-day cadence during Phase I but transitioned to a two-day cadence thereafter (Bellm et al. 2019a). This analysis makes use of both the public and partnership datasets up to September 2024. On a typical full night, ZTF generates between 600,000 and 1.2 million alerts (Masci et al. 2019; Patterson et al. 2019). As a result, ZTF is a powerful tool for discovering and monitoring transients, making it particularly well-suited for building large, homogeneous samples of SNe essential for training machine learning models.

The Bright Transient Survey (BTS; Fremling et al. 2020; Perley et al. 2020) is a dedicated program within ZTF that aims to spectroscopically classify all extragalactic transients, excluding active galactic nuclei (AGN), with a peak brighter than 18.5 magnitude. This is achieved using low-resolution spectra from the Spectral Energy Distribution Machine (SEDM) that operates on the Palomar 60-inch telescope (Blagorodnova et al. 2018; Rigault et al. 2019; Kim et al. 2022). This constitutes the majority of the classified sources in the ZTF dataset, and is the largest brightness-limited SN survey to date. As well as relying

on human scanners to request follow-up, BTS employs several machine learning classifiers to automate classification. SNIascore (Fremling et al. 2021) specialises in real-time classification of SNe Ia from SEDM spectra, achieving $<0.6\%$ false-positive rates. CCSNscore (Sharma et al. 2025) extends this framework to core-collapse SNe, whilst also incorporating ZTF light curves, to distinguish SNe II from SNe Ib/c with high accuracy. BTSpot (Rehemtulla et al. 2024) is a discovery-to-classification pipeline that autonomously triggers follow-up observations and processes data through these classifiers, enabling automated reporting of ZTF SNe.

The majority of our dataset consisted of the BTS SN sample² collected up to September 2024, although additional ZTF objects were included to increase the diversity in our SLSN class (see Sect. 2.1 for details). We obtained the list of classified transients and their corresponding classifications, redshifts, right ascensions, and declinations using the internal BTS Sample Explorer³, selecting all classified supernovae regardless of peak magnitude. The forced photometry (FP) for our sample was acquired using the IPAC ZTF forced photometry service (Masci et al. 2023), including both public and partnership data. We then processed the data to remove the baseline (i.e. the background flux level at the transient's location) using the alert processing software AMPEL (Nordin et al. 2019)⁴. Transient light that may be present in the reference image is largely removed during the baseline subtraction. We also removed unreliable data points from the FP light curves using warning flags from the IPAC service, which indicate issues with the science image, poor seeing, or baseline calculation.

2.1. Class breakdown

We trained our model on the following classes of SNe: SN Ia, SN Ib/c, SN II, SN IIn, and SLSN. Table 1 lists how individual subtypes were grouped into these classes, along with their sample sizes. Table 2 shows the SN subtypes that were excluded from the model training. We included 91T-like SNe Ia in our SN Ia sample because, although they are slightly more luminous than normal SNe Ia, they are generally well modelled by standard SN Ia light curve models, and their peculiarity is primarily spectroscopic (Dimitriadis et al. 2025).

We note that some peculiar SNe Ia are likely still present in our training sample due to incomplete or ambiguous subtyping, which may affect classification performance. The redshifts and classifications are preliminary, as they come from an internal database, and are being finalised within the BTS working group (Qin et al., in prep.). Additionally, there are updated SN Ia subtypes presented in the ZTF SN Ia DR2 publications (Rigault et al. 2025; Dimitriadis et al. 2025; Burgaz et al. 2025), which will be incorporated in future work.

We excluded both peculiar and uncommon transient subtypes from our model training due to insufficient sample sizes to reliably model their behaviour, which could otherwise bias the classifier. For example, SNe I Ib are known to be photometrically distinct from other SNe II (e.g., Pessi et al. 2019). TDEs were also excluded because of their limited sample size. Additionally, SNe Ia with the “Ia?” label in the BTS internal catalogue, indicating uncertain classification, were removed. We also expect that K-corrections (see Sect. 3.2) would be less accurate for the

² This will be released in Qin et al. (in prep.)

³ A public version of the catalogue is available at: sites.astro.caltech.edu/ztf/bts/explorer.php

⁴ ZTFIPACForcedPhotometryAlertSupplier.py

peculiar subtypes due to their different spectral properties. However, we discuss how such excluded events would be classified by our model in Sect. 5.4.

Furthermore, we incorporated an additional sample of SLSNe to increase the diversity of the training sample, since the original BTS sample only contained 154 objects. We included classified events from Chen et al. (2023) for SLSNe-I and Kangas et al. (2022) and Pessi et al. (2025) for SLSNe-II. We also queried Fritz, a SkyPortal platform for members of the ZTF collaboration (van der Walt et al. 2019; Coughlin et al. 2023), for additional SLSN candidates not included in the previous ZTF publications. This increased our SLSN sample by 84 objects.

Table 1: Classes included from the BTS sample and additional SLSN samples, and their corresponding SN subtypes.

Class	Class total (%)	Subtypes	Subtypes total
SN Ia	6614 (69.4%)	Ia and Ia-norm	6396
		Ia-91T	218
SN Ib/c	551 (5.8%)	Ib	220
		Ib/c	43
		Ic	213
SN II	1859 (19.5%)	Ic-BL	75
		IIL	2
		IIP	173
SLSN	238 (2.5%)	SLSN-I	155
		SLSN-II	79
		SLSN-I.5	4
SN IIn	271 (2.8%)	IIn	271

Table 2: SN subtypes excluded in training.

Class	Class total	Subtypes	Subtypes total
SN Ia	254	Ia?	35
		Ia-pec	41
		Ia-CSM	28
		Ia-91bg	86
		Ia-99aa	1
		Ia-00cx	3
		Iax (Ia-02xc)	38
		Ia-03fg	21
		Ia-18byg	1
SN Ib/c	42	Ib-pec	4
		Ibn	36
		Icn	2
SN II	163	IIb	160
		IIb-pec	1
		II-pec	2
TDE	42	TDE	42

2.2. Training and test samples

We trained our models using a 90% training and 10% test split. To assess model performance across different magnitude regimes, we divided the dataset into the following subsamples.

2.2.1. BrightZTF and FaintZTF

We split the data by class (as defined in Table 1) into the brightest 90% – referred to as BrightZTF – and the faintest 10% –

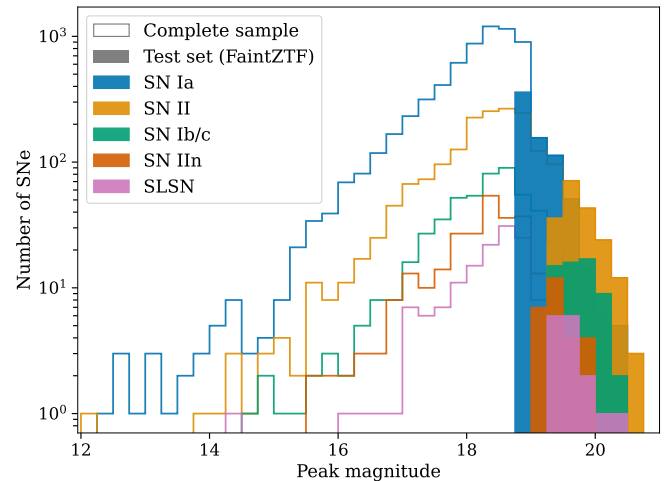


Fig. 1: The peak apparent magnitude distribution for our sample, divided into classes of SN Ia (blue), SN II (orange), SN Ib/c (green), SN IIn (red), SLSN (pink). The filled histograms represent the test sample, FaintZTF, and the outline represents the full dataset. The peak apparent magnitude corresponds to the brightest detection in any ZTF band (g , r or i).

referred to as FaintZTF – based on peak apparent magnitude (using the brightest detection in any band). This is illustrated by the peak apparent magnitude distribution shown in Fig. 1, where the filled histograms represent FaintZTF and the outline shows the complete dataset. In practice, FaintZTF is utilised as the test set, and additional quality cuts (described in Sect. 4.1) are applied before we perform the classifications. This setup provides a benchmark for evaluating the effectiveness of our data augmentation in improving classifier performance at fainter magnitudes. When augmentation is applied to these samples, we refer to them as BrightZTF+Noise and FaintZTF+Noise.

2.2.2. RandomZTF

To evaluate performance across a broader magnitude range, we also perform a random split of the data – referred to as RandomZTF. In this case, we generate five different training and test sets using five random seeds, and report the average classification score. When augmentation is applied to these samples, we refer to them as RandomZTF+Noise.

3. Augmentation method

To create a training sample that is more representative of the test sample, we implemented an augmentation method that generates fainter, noisier synthetic light curves. This is similar to the methodology of Boone (2019), where redshifts are resampled, except we did not include Gaussian Process fitting to our light curves. Instead, we accurately modelled the behaviour of the ZTF flux errors in different magnitude regimes and scaled our flux and flux error values accordingly (Sect. 3.1). We also implemented K-corrections (Sect. 3.2) and additional augmentation methods such as removing data points (Sect. 3.3).

3.1. Modelling the ZTF flux errors at higher redshifts

To accurately generate the errors for the augmented light curves, we determined an error model for the ZTF data by attempting to simulate the flux errors from the original sample of ZTF light curves. We start by assuming that the dominant contributions to the true flux error, σ_t , are due to the Poisson counting of the photons ($\sigma_t \propto \sqrt{f_t}$, where f_t is the true flux) and a bias term that is dominant at lower flux values, e_b (where $\sigma_t \propto e_b$). Then, the variance of the true flux error would be

$$\sigma_t^2 = f_t + e_b^2. \quad (1)$$

When comparing this with the ZTF data, we found that this does not capture the true nature of the noise, particularly at lower flux values. In ZTF photometry, the actual noise affecting a measurement arises from a combination of statistical, systematic, and environmental factors, not just Poisson noise from the source photons. One important component is sky background noise, which results from Poisson fluctuations in the sky brightness, including contributions from moonlight. Because this background is integrated within the PSF aperture, it adds a flux-dependent noise term that varies with observing conditions (e.g., lunation and airmass). Calibration issues such as zeropoint drift, PSF mismatches, and astrometric misalignments also introduce uncertainties that are not purely random, but often correlated in space, time, or observing conditions. These effects are further compounded in difference imaging, particularly for transients in bright host galaxies, where host light may be incompletely subtracted, leaving behind spatially variable residuals that contaminate the transient signal. While the noise properties can vary somewhat between filters due to different throughput and sky brightness levels, we adopt a single model across all three ZTF bands (g, r, i) as a simplification, since the dominant sources of noise exhibit similar qualitative behaviour across filters. Overall, these contributions combine to produce measurement uncertainties that are neither strictly Poissonian nor entirely uncorrelated, motivating the use of an empirical noise model to approximate the observed errors in real ZTF light curves.

To account for these effects, we introduce two empirical fitting terms: a random exponential component, ϵ , and a constant offset, δ . This results in the following relationship between flux and flux error:

$$\frac{\sigma_t}{f_t} = \sqrt{\frac{1}{f_t} + \frac{e_b^2}{f_t^2} + \epsilon + \delta}, \quad \epsilon \sim \text{Exp}(\lambda_f), \quad (2)$$

where the rate parameter of the exponential distribution is linearly dependent on the flux such that $\lambda_f = m \cdot f_t + c$.

Due to the correlated nature of the error model in Equation 2, it is not possible to determine the optimal values of the parameters (e_b, m, c, δ) through minimisation or maximum-likelihood methods. Instead, we fit the underlying, deterministic model in Equation 1 to the original ZTF light curves⁵, to recover the parameter e_b . We then subtracted this model from the data to study the behaviour of the remaining noise. The left panels of Fig. 2 show the distribution of σ_t/f_t for the ZTF sample, with the residual distribution for ϵ shown in the lower panel. As illustrated in Fig. 3, we fit an exponential curve to the ϵ component of the data in flux bins to determine the parameters m and c . Finally, we

⁵ Throughout this work, we use the term “flux” for consistency with common usage in optical astronomy, although our measurements are in flux densities. These are expressed in janskys and scaled to be consistent with the AB magnitude system.

compared the simulated data to the real data at different flux bins to determine the offset parameter δ . This is illustrated in Fig. 4, for binned data in the low ($f_t < 400$), medium ($800 < f_t < 1200$), and high ($f_t > 1600$) flux value ranges. This process was repeated iteratively until the optimum parameters were derived, which are given as $e_b = 18.0$, $m = 0.04$, $c = 4.7$, $\delta = -0.006$.

Figure 2 shows a comparison of the σ_t/f_t vs. f_t distributions of the original ZTF light curves and the ZTF light curves with flux errors simulated according to Equation 2. We note that the errors are slightly underestimated at the lower flux range of $f_t < 400$, which can also be seen in the left panel of Fig. 4. In particular, Fig. 4 shows that this primarily affects measurements with $\sigma_t/f_t > 0.2$, which corresponds to data points with a signal-to-noise ratio (SNR) of less than five. This is likely because the noise is not purely exponential within this range, as shown in the bottom left panel of Fig. 3, where the exponential curve is a poorer fit in the $f_t < 400$ flux bin. This could be addressed by including an additional random Gaussian component dependent on f_t in the error model, but this was not implemented since the parameter optimisation would become too complex. Data points with low SNRs are effectively downweighted by the model during both training and inference, so they are unlikely to strongly influence the results.

Using our empirically-determined error model, we can simulate how the flux uncertainties would appear if an object were observed at a higher redshift. To approximate the corresponding flux values under these conditions, we apply a redshift-motivated scaling to the light curves. Specifically, we define:

$$f_z = D f_t, \quad \text{where} \quad D = \frac{D_L(z_{\text{true}})^2}{D_L(z_{\text{sim}})^2}, \quad (3)$$

with D_L the luminosity distance. This is computed assuming a flat Λ CDM cosmology with parameters from [Planck Collaboration et al. \(2020\)](#): $H_0 = 67.7 \text{ km s}^{-1} \text{ Mpc}^{-1}$ and $\Omega_M = 0.310$. The D_L^2 factor accounts for luminosity-distance dimming, since the observed flux of a source with fixed intrinsic luminosity scales as $F \propto D_L^{-2}$. We separately compute K-corrections to account for the shifting of the observed bandpass relative to the rest-frame spectral energy distribution (SED) using spectral templates (see Sect. 3.2), and apply these as an additive magnitude offset after flux scaling.

While this formula does not attempt to model the full redshift transformation (including, e.g., time dilation of the observation dates), it provides an approximation of redshift evolution that captures the dominant dimming effect without altering the cadence of the light curve. This enables consistent training and evaluation of classification models with light curves at similar epochs but varying SNR. Additionally, the majority of transients in our sample lie at relatively low redshifts ($z \lesssim 0.2$), and our simulated redshift shifts are modest ($z_{\text{sim}} - z_{\text{true}} \leq 0.1$), corresponding to time dilation effects of less than $\sim 10\%$. These effects are typically subdominant compared to photometric uncertainties and cadence limitations.

Combining Equations 2 and 3, the scaling of the flux uncertainties when transforming a measured flux f_t at redshift z_{true} to the simulated flux f_z at z_{sim} is given by

$$\frac{\sigma_z}{\sigma_t} = \frac{\sqrt{D f_t + e_b^2} + D f_t (\epsilon + \delta)}{\sqrt{f_t + e_b^2} + f_t (\epsilon + \delta)}. \quad (4)$$

The new flux error, σ_z , is obtained by multiplying the original flux error by the factor in Equation 4.

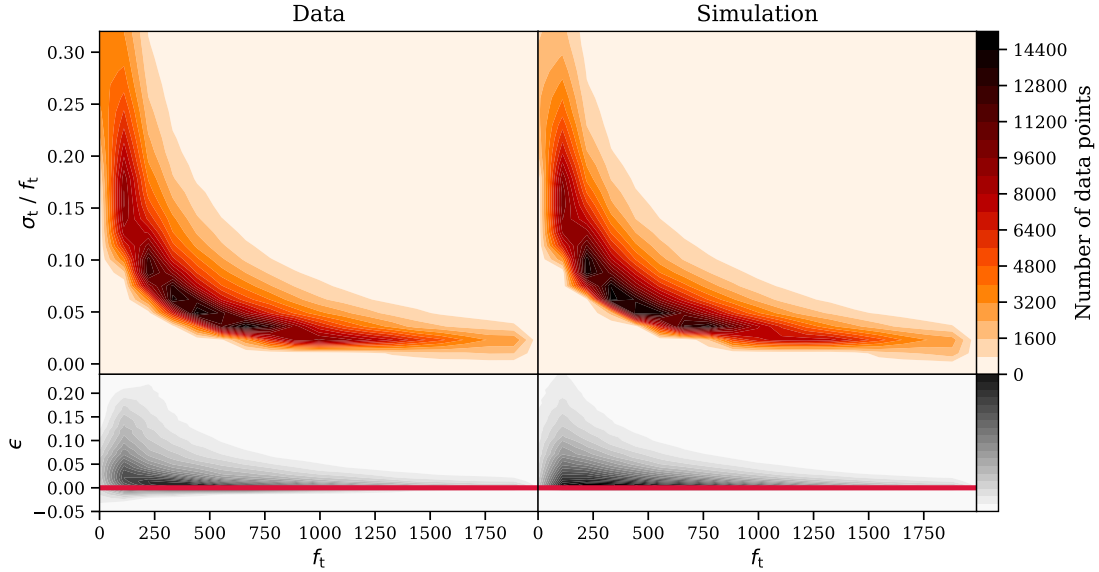


Fig. 2: Comparison of the σ_t/f_t vs. f_t distributions of the original ZTF light curves (upper left) and the ZTF light curves with flux errors simulated according to Equation 2 (upper right). The corresponding residual distributions for ϵ are shown in the lower panels.

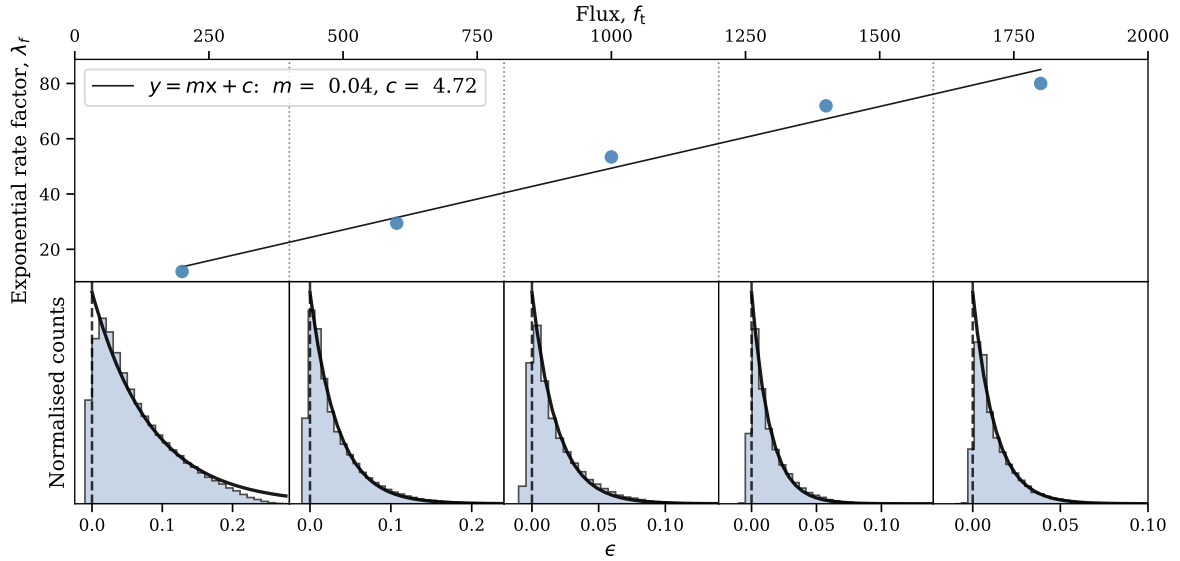


Fig. 3: Flux evolution of the random exponential component to the noise, ϵ . The lower panels show histograms of ϵ for flux bins of width 400. The upper panel shows the corresponding exponential scale factor, λ_f , for each flux bin, which is fit with a linear model, $\lambda_f = m \cdot f_t + c$.

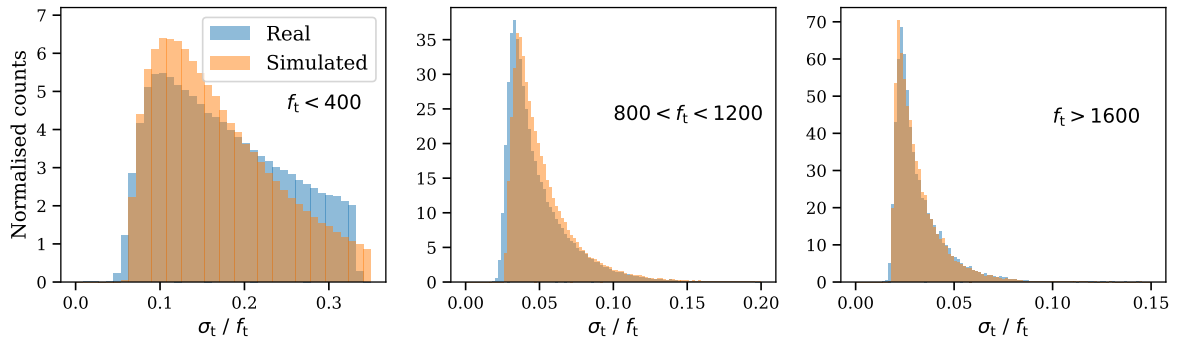


Fig. 4: Comparison of the simulated and real σ_t/f_t values at flux bins in the low ($f_t < 400$), medium ($800 < f_t < 1200$), and high ($f_t > 1600$) flux regimes.

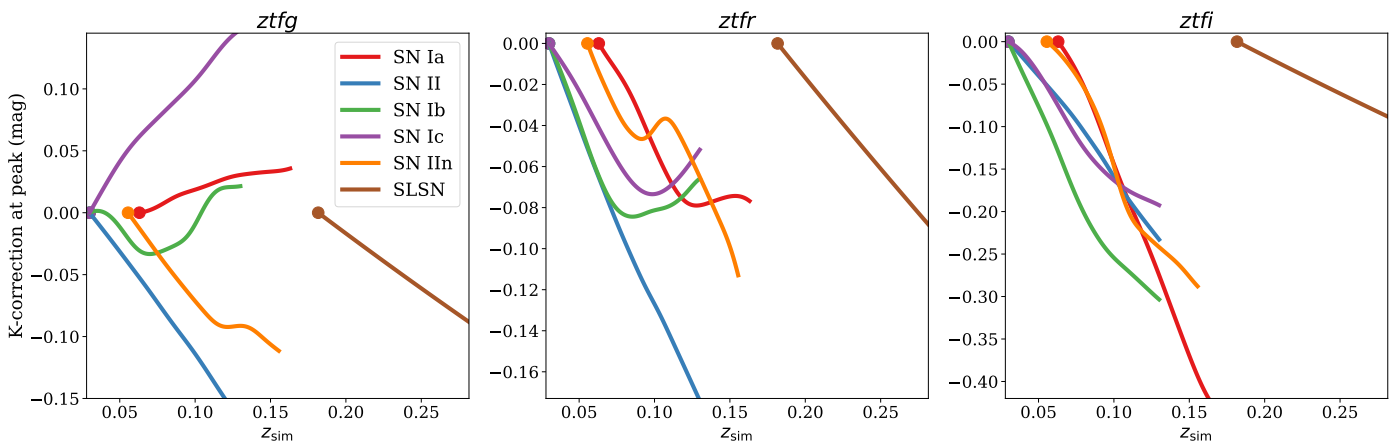


Fig. 5: K-corrections at peak brightness for the three ZTF bands (g : left, r : centre, i : right), applied to a representative set of SN types. For each class, the true redshift z_{true} (indicated by a dot at $(z_{\text{true}}, 0)$) is taken as the median redshift from the BTS catalogue. Corrections are shown over the range $z_{\text{sim}} \in [z_{\text{true}}, z_{\text{true}} + 0.1]$. Template corrections are shown for SNe Ia (red), II (blue), Ib (green), Ic (purple), and IIn (orange), alongside the constant approximation adopted for SLSNe (brown).

3.2. K-correction

A K-correction is the conversion of flux measured in an observer-frame passband to flux in a rest-frame passband, accounting for the shift in wavelength at different redshifts (Oke & Sandage 1968). We applied a K-correction during redshift augmentation to account for the shift in rest-frame wavelength at higher simulated redshifts. This was performed using spectral templates from `sncosmo` (Barbary et al. 2022)⁶, where available.

The source model was constructed using an `sncosmo` template, selected according to the SN type (see Table A.1 in the Appendix for details on the specific templates used). For the non-parametric models (i.e., all except the SALT2 model used for SNe Ia), we did not need to choose specific parameter values, since we compute a relative quantity and the model amplitude cancels in the K-correction. For the SALT2 model (Guy et al. 2007; Betoule et al. 2014), we fixed the parameters to $[x_1, c, M_B] = [1.0, 0.2, -19.4]$. While individual SNe within each class can exhibit spectral diversity (particularly in colour for core-collapse SNe, and in both light curve shape and colour for SNe Ia), these templates provide a reasonable approximation for capturing average K-correction behaviour across the population. K-corrections were determined for each object by computing the difference between the model-predicted observed flux at the original redshift (z_{true}) and the simulated redshift (z_{sim}).

There are no templates available for SLSNe in `sncosmo`, due to their diverse and variable spectral properties. Instead, we relied upon an approximation of the K-correction formulae described in Hogg et al. (2002), where we would expect a constant correction of $-2.5 \log(1+z)$ mag. Previously, Chen et al. (2023) showed that this approximation is comparable to K-corrections computed from spectra for SLSNe-I observed by ZTF. Therefore, we applied a correction of

$$K = -2.5 \log \left(\frac{1 + z_{\text{sim}}}{1 + z_{\text{true}}} \right) \quad (5)$$

when we transform our SLSN light curves from z_{true} to z_{sim} .

Figure 5 illustrates the K-corrections at peak brightness for the three ZTF bands, applied to a representative set of SN types.

For each class, the true redshift z_{true} is taken as the median redshift in the BTS catalogue, and corrections are shown over the range $[z_{\text{true}}, z_{\text{true}} + 0.1]$ in simulated redshift z_{sim} . The approximation used for SLSNe is justified, since the K-corrections across different SN types are broadly similar in magnitude. We also note that the i -band exhibits the largest corrections, though this is unlikely to significantly affect our results due to the relatively sparse i -band sampling.

3.3. Noisification

In this subsection, we outline the method for adding noise to the light curves, a technique referred to as ‘noisification’. This involves selecting specific augmentation parameters to generate different versions of the training data. The evaluation of these parameter choices is presented in Sect. 5.1, where we selected the optimal augmented datasets for our final models.

First, we selected a new redshift value by sampling within the range $z_{\text{sim}} \in [z_{\text{true}}, z_{\text{true}} + 0.1]$, using a probability distribution proportional to $z^{\text{z_scale}}$, where $\text{z_scale} \in \{0, 2\}$. We tested two distributions: for $\text{z_scale} = 0$, the distribution is flat, implying no preference across the interval; for $\text{z_scale} = 2$, the distribution reflects the expected scaling of SNe in the low-redshift universe ($z \lesssim 0.3$), assuming a constant volumetric SN rate. In this regime, the number of observed SNe scales with the comoving volume element, $dV \propto z^2 dz$. The choice of $\text{z_scale} = 2$ preferentially samples higher redshifts within the interval.

Next, we generated a simulated light curve from the new redshift value. We calculated the new flux error, σ_z , by multiplying the observed flux error by the scale factor in Equation 4, as described in Sect. 3.1. The new flux value, f_z , is the sum of the scaled flux and a Gaussian scatter term, given by $f_z = D f_t + \mathcal{N}(0, \sigma_z^2)$, where D is defined in Equation 3. This procedure adds simulated noise on top of the original measurement uncertainties, resulting in slightly higher total scatter than a real observation at the simulated redshift. However, since the original noise cannot be disentangled from the observed flux, removing it is not feasible. This conservative approach ensures we do not underestimate uncertainties when simulating higher-redshift observations. A K-correction term was also applied, as described in Sect. 3.2.

⁶ sncosmo.readthedocs.io

We applied quality cuts to the simulated light curves, requiring the peak detection to have an SNR greater than five. Furthermore, each light curve was required to contain at least five detections with an SNR greater than five. Simulated light curves that did not meet these criteria were excluded from the training sample.

To ensure that the simulated light curves remain diverse, even when generating hundreds of copies, we applied additional augmentation by removing data points. This was done using two approaches: based on local density or via random subsampling. For the density-based method, we computed the number of detections per band within a rolling five-day window. If the local density within a window exceeded a user-defined threshold, called `cadence_scale`, data points were dropped at random with a uniform probability. We tested two values for `cadence_scale`: 0.5 (corresponding to one detection every two days per band) and 100 (which results in no density-based dropping). For random subsampling, the parameter `subsampling_rate` specifies the fraction of data points retained. We only removed data points randomly if there were more than 10 detections in any band. For the `subsampling_rate`, we tested values of 0.7, 0.9, and 1.0 (i.e., no subsampling).

Figures B.1 and B.2 in the Appendix present examples of an augmented SN Ia and SN II, respectively. For comparison, each panel also includes a real light curve at a similar redshift, illustrating that the augmented light curves exhibit realistic brightness evolution and scatter consistent with real observations.

3.4. Testing the noisification with SALT2 fits to SNe Ia

As an additional test of our error model, we compared SALT2 fits to the original SN Ia sample and an augmented version of the same sample. The SALT2 model (Guy et al. 2007) is a light curve template that characterises SNe Ia using two parameters: stretch (x_1) and colour (c). In addition to these, the model includes a normalisation factor x_0 , which determines the overall brightness of the SN, and a time of peak brightness t_0 . We performed the fits using `sncosmo` (Barbary et al. 2022), implementing SALT2 version 2.4 as trained by Betoule et al. (2014).

We followed the procedure described in Sect. 3.3 to generate an augmented copy of each SN Ia using the following augmentation parameters: `z_scale` = 2, `cadence_scale` = 100, `subsampling_rate` = 1 (i.e., we did not manually remove data points). For each fit, we defined the initial parameters for the SALT2 fit as follows: $t_0 = t_{0,\text{est}}$, $x_0 = 1.0$, $x_1 = 0.0$, $c = 0.0$, where $t_{0,\text{est}}$ is estimated as the time of the brightest detection in any filter. We also restricted the fitting window to the rest-frame phase range $t \in [-20, 50]$, which corresponds to the model limit of SALT2. Fits were performed on both the original and augmented light curves, and the corresponding reduced χ^2 values were calculated.

A comparison of the reduced χ^2 values from the SALT2 fits to the original and augmented samples is shown in Fig. 6, where we further divide the ZTF sample into bright ($m < 18.5$) and faint ($m > 18.5$) subsamples. This division highlights differences in the reduced χ^2 distributions: the brighter SNe Ia tend to exhibit larger values and a broader overall distribution. This is likely due to calibration issues, such as detector nonlinearity, which introduce systematic errors. These systematics have a greater impact on the light curves of brighter objects because of their higher SNRs, whereas fainter, noise-dominated light curves are less affected by these systematics due to their larger observa-

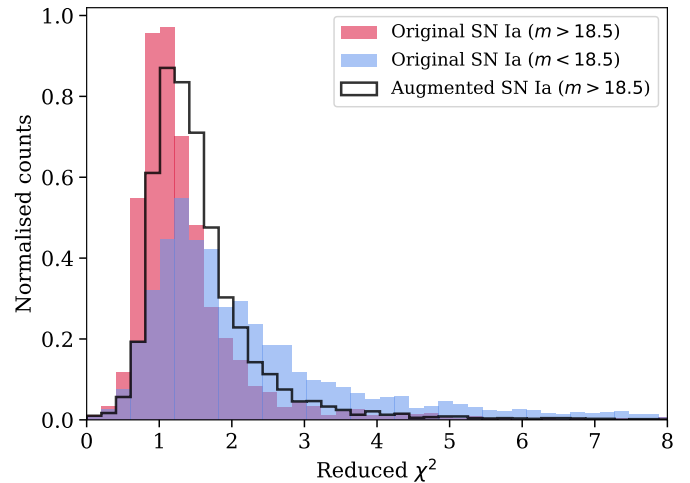


Fig. 6: Comparison of the reduced χ^2 values from SALT2 fits to the original ZTF SN Ia sample – divided into bright (blue) and faint (red) subsamples – and to the augmented copies of the same sample (black outline).

tional uncertainties. We also show the augmented sample, limited to objects with $m > 18.5$.

We note that the distribution of reduced χ^2 values for the augmented sample is in reasonable agreement with that of the faint ZTF subsample. However, the augmented sample has a slightly higher median reduced χ^2 (1.39 compared to 1.18), likely due to underestimated errors at low fluxes, as discussed in Sect. 3.1. Additionally, as discussed in Sect. 3.3, the augmented light curves include both the original measurement noise and additional simulated scatter, which may slightly overestimate the total scatter. It is also possible that this discrepancy arises from the broader and fainter magnitude range of the augmented SNe Ia. As the SNR decreases near the ZTF detection limit, the number of significant detections, and thus the degrees of freedom in the SALT2 fit, tends to decrease, which can inflate the reduced χ^2 . Overall, these results suggest that our noisification method produces realistic ZTF light curves at higher redshifts.

4. Classification procedure

In this section, we describe the generation of the training and test samples. We then detail how the training sample was used to train a ParSNIP model that captures transient behaviour. Finally, we explain how features extracted from the trained ParSNIP model were used to train a classifier and classify the test sample.

4.1. Generating the training and test samples

First, we divided the data into training and test samples, as described in Sect. 2.2. This split is performed before any augmentation to ensure that no copies of the same object appear in both sets.

We next determined the number of augmented copies to generate per ZTF object, based on its class. We tested three augmentation strategies: (1) balanced, where the number of objects in each class is equalised by generating more copies of underrepresented classes (e.g., significantly more SLSNe than SNe Ia); (2) unbalanced, where a constant number of augmented copies is created per class, preserving the original class imbalance; and

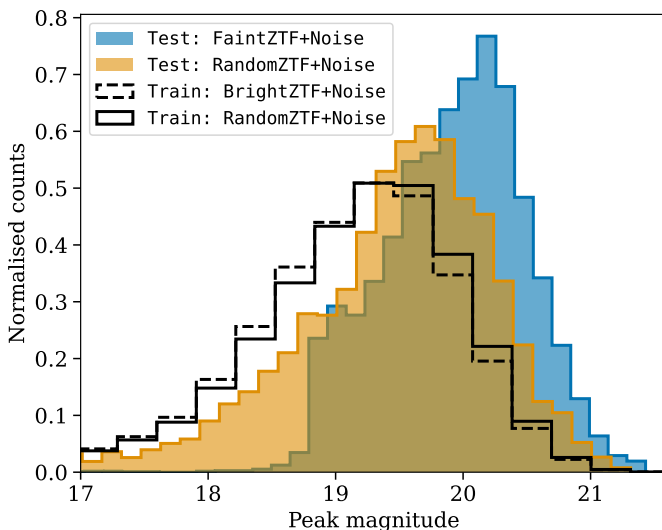


Fig. 7: Comparison of training and test peak apparent magnitude distributions between the BrightZTF/FaintZTF and a representative RandomZTF split (one random seed shown). The training samples were augmented using the parameters shown in bold in Table 3.

(3) hybrid, where non-Ia classes are balanced, but approximately five times more SNe Ia are generated, with the goal of improving the classifier’s ability to distinguish them from other types.

Before augmentation, we imposed phase limits based on the peak date from the BTS catalogue (defined as the date of the brightest detection in any filter), to exclude FP data well outside the transient event, such as remaining pre- or post-explosion baselines or spurious detections. For longer-lived classes such as SLSNe and SNe IIn, we used a phase range of $t \in [-100, 200]$ days relative to peak; for all other classes, the range was $t \in [-50, 80]$ days. While these cuts do not explicitly provide the classifier with information about the transient’s true duration or peak date, the longer phase range for SLSNe and SNe IIn means that their light curves typically include data over a longer timespan. Consequently, the classifier could indirectly infer the longer duration characteristic of these classes based on the extent of the observed light curve. However, this information is a physically meaningful feature of the transient rather than an explicit input, and the model still relies on the photometric data itself to distinguish classes.

Each training light curve was augmented as described in Sect. 3.3. We aimed to generate the required number of augmented light curves, but this was sometimes not possible for objects that were already faint. If a light curve passing the SNR cuts was not produced within the first 50 iterations or during any subsequent 2000 consecutive iterations, we stopped the process and moved on to the next object.

We applied the same augmentation methodology to the test light curves but fixed the augmentation parameters to ensure each test sample was identical, allowing direct comparison of model performance. We used the following augmentation parameters, as in Sect. 3.4: `z_scale = 2`, `cadence_scale = 100`, `subsampling_rate = 1`. For class scaling, we used an unbalanced dataset with 10 copies per class to preserve the original class imbalance, reflecting a more realistic distribution. We also chose `z_scale = 2` to better reflect the expected redshift distribution.

Furthermore, we imposed additional quality cuts on the original test data prior to augmentation, requiring more than five detections with an SNR of greater than five, a duration (defined as the time span between its first and last detection) exceeding 20 days, and observations in at least two bands, each with a minimum of two detections. These cuts were motivated by the requirement for light curves suitable for cosmological analyses.

Figure 7 shows the peak apparent magnitude distributions for the different training and test configurations, highlighting the fainter magnitude range in the FaintZTF+Noise test sample. While the BrightZTF+Noise training set is slightly skewed toward brighter magnitudes, its distribution is broadly similar to that of the RandomZTF+Noise training set.

4.2. Training the ParSNIP model and classifier

We trained ParSNIP models using our training datasets, following a methodology similar to Boone (2021). ParSNIP is a modified version of a variational autoencoder (Kingma & Welling 2013) that is designed to capture the diverse behaviour of transients using a low-dimensional latent space. Its architecture includes a neural network that encodes each light curve into three intrinsic latent parameters, referred to as s_1 , s_2 , and s_3 , which describe the intrinsic spectrum of a given transient. There is an additional component, denoted the ‘physics layer’, which models how the light from the transient would be observed, by incorporating explicit latent variables (a reference time t_0 , amplitude of the light curve A , and the colour c) along with observational metadata (redshift z , observation time t , and bandpass B). The physics layer enables ParSNIP to learn a representation of each transient that is invariant to observing conditions, such as redshift. Figure 8 illustrates how two of the intrinsic latent parameters, s_1 and s_2 , vary across the different classes in our model.

To train the model, we adopted the hyperparameters from Boone (2021), who found that model performance is generally insensitive to these settings. We used the Adam optimiser (Kingma & Ba 2014) with an initial learning rate of 10^{-3} and a batch size of 128 light curves. The learning rate was reduced by a factor of 0.5 if the loss function did not improve after 10 epochs, continuing until the learning rate dropped below 10^{-5} . Consistent with Boone (2021), we found that models typically converged after approximately 300 epochs, although this varied considerably across training runs.

After training the model, we extracted the ParSNIP features for both the training and test samples. These features were then used to train a classifier using the gradient-boosted decision tree framework LightGBM (Ke et al. 2017). Following the approach of Boone (2019), we adopted the default hyperparameters, employed 10-fold cross-validation, and set the `min_child_weight` parameter to 100 to prevent any overfitting to the augmented light curves. The classification features include colour, luminosity, amplitude, the three latent variables, their associated uncertainties, and the uncertainty in the reference time. ParSNIP also outputs the total number of detections, along with counts of detections with $\text{SNR} > 3$ and > 5 across three epochs: 50 days before peak, 50 days after peak, and all following days. These values were included as additional classifier features.

Our primary classifier was a binary model distinguishing SNe Ia from all other types, outputting the probability that a given object is an SN Ia. We also tested multi-class classifiers, which assign probabilities that an object belongs to each class in the training set: SN Ia, SN Ib/c, SN II, SN IIn, and SLSN.

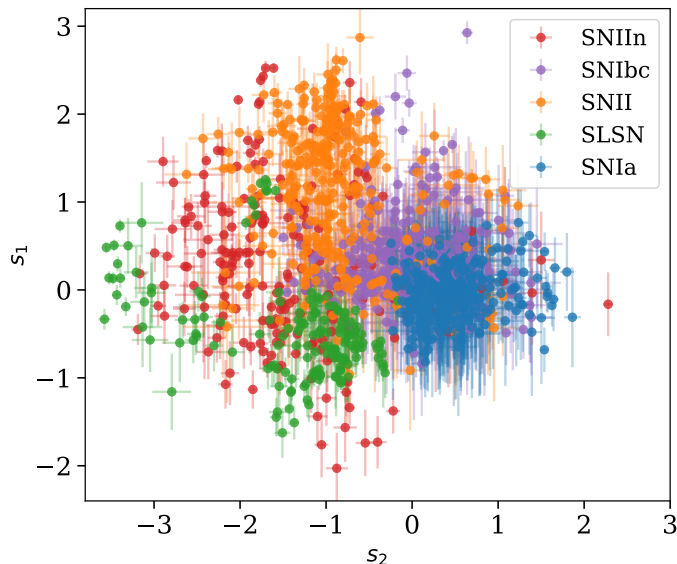


Fig. 8: Distribution of transient classes in the intrinsic latent space defined by the s_1 and s_2 parameters of the trained ParSNIP model. Each point represents a light curve from the augmented FaintZTF+Noise test sample, coloured by class: SN Ia (blue), SN II (orange), SN Ib/c (purple), SLSN (green) and SN IIn (red). The separation between classes emphasises the model’s ability to distinguish between transient types, though some overlap remains (e.g., between SLSNe, SNe II, and SNe IIn, or between SNe Ia and SNe Ibc).

5. Results and discussion

In this section, we present the results of our classification procedure. We begin by describing the optimisation of the augmentation parameters (Sect. 5.1) and show the results from one of our best-performing models (Sect. 5.2). We then evaluate the classifier on additional datasets, including the ZTF SN Ia DR2 sample (Sect. 5.3) and the peculiar or uncommon subtypes from BTS that we initially excluded (Sect. 5.4). Finally, we discuss potential applications of our method in supernova cosmology (Sect. 5.5) and real-time survey classification (Sect. 5.6).

The primary metrics used to evaluate classifier performance are recall (also referred to as efficiency or completeness, the fraction of the real events we correctly identify) and precision (also referred to as purity, the fraction of predicted positive classifications that are correct). These are defined as:

$$\text{recall} = \frac{\text{TP}}{\text{TP} + \text{FN}}, \quad \text{precision} = \frac{\text{TP}}{\text{TP} + \text{FP}}, \quad (6)$$

where TP is the number of true positives, FN is the number of false negatives, and FP is the number of false positives. Throughout multiple iterations, we observed a trade-off between SN Ia recall and the recall of other classes – improvements in one often led to declines in the other. Given the context of our work, we prioritised SN Ia recall, as discussed in Sect. 1.1, since this metric has a more direct impact on the effectiveness of SN Ia cosmology analyses.

As described in Sect. 2.2, we trained and tested on different samples to evaluate the robustness of our models. We followed two main strategies: (1) training on BrightZTF or its augmented counterpart, BrightZTF+Noise, and testing on FaintZTF or FaintZTF+Noise; and (2) training and testing on a 90%/10% split of RandomZTF+Noise.

5.1. Augmentation parameter optimisation

We tested various augmentation parameters (described in Sects. 3.3 and 4.1) to identify which values produced the best classification performance. The tested parameters and their values are listed in Table 3. We evaluated model performance using the FaintZTF and FaintZTF+Noise test sets, focusing exclusively on results from the binary SN Ia classifier. The primary metrics were the mean SN Ia recall and the mean SN Other recall, averaged over both test sets.

Table 3: Summary of augmentation parameter configurations tested in this study.

Parameter	Values
Class scale	Balanced: 2, 3, 4, 5 Unbalanced: 2, 5, 10, 15 Hybrid: 10
z_scale	0 , 2
cadence_scale	0.5, 100
subsampling_rate	0.7, 0.9 , 1

Notes. The bolded values indicate the parameters of the best models discussed in Sect. 5.2.

For balanced class scaling, the number of SN Ia augmentations is set by the scaling factor (e.g., a scale of 3 produces three versions per SN Ia), and all other classes are upsampled to match this total, resulting in equal numbers of objects per class. In the unbalanced setting, the same number of augmentations is applied to each object across all classes (e.g., scale = 5 produces five versions per object, regardless of class). The hybrid strategy generates 10 versions per SN Ia, while the remaining classes are augmented to approximately match a sample in which each class contains twice the original number of SN Ia objects. In other words, the hybrid scaling generates five times as many SN Ia as each of the other individual classes.

We found that class scaling had the greatest impact on classification performance, highlighting the effectiveness of augmentation in improving the classifier. As shown in Fig. 9, the mean SN Ia recall increases with the number of SNe Ia generated. Among the strategies tested, the hybrid approach achieved the best average performance, followed by the balanced class scaling. Conversely, the unbalanced class scaling produced the highest average SN Other recall.

We also observed a weaker dependence on the cadence_scale and subsampling_rate parameters. This is illustrated for the balanced classes in Figs. C.1 and C.2 in the Appendix, where the average SN Ia recall was highest when no data points were removed, while the average SN Other recall improved with more aggressive subsampling.

Introducing scatter in the observation times of the detections was also tested. However, even small perturbations (e.g., 0.1 days, or approximately 2.4 hours) degraded the SN Ia precision. This effect likely arises because the temporal offsets shift the observed fluxes in different bands relative to each other, altering the inferred colours and the shape of the light curves. Since classification relies on subtle differences in colour evolution and light curve features, these shifts can increase confusion with SNe Ib/c.

5.2. Classification results

After evaluating different augmentation parameters in Sect. 5.1, we selected the model configuration corresponding to the bolded

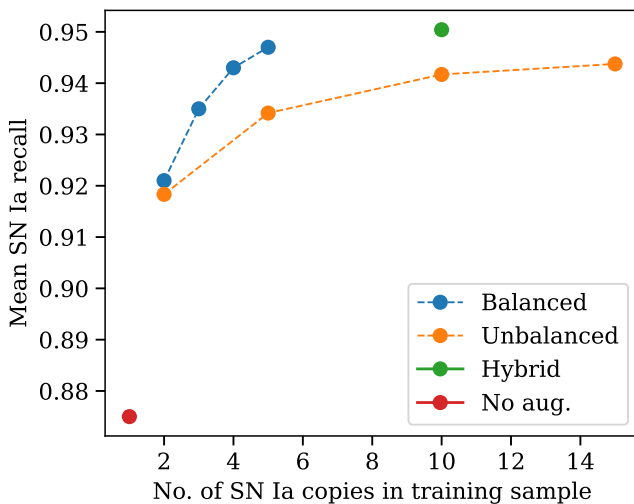


Fig. 9: Mean SN Ia recall (averaged over multiple iterations of the FaintZTF and FaintZTF+Noise test sets) as a function of the number of SNe Ia we generate in the BrightZTF+Noise training sample. Results are shown for the different class scaling strategies described in the main text: balanced (blue), unbalanced (orange), and hybrid (green). For comparison, we also include a model trained without augmentation (i.e., on BrightZTF only), denoted ‘no aug.’ (red), to illustrate the benefit of augmentation.

parameters in Table 3. To demonstrate the robustness and generalisability of our classification model, we present four scenarios:

- (i) training and testing on the original, unaugmented data (Train: BrightZTF, Test: FaintZTF),
- (ii) training on original data but testing on augmented (noisier) light curves (Train: BrightZTF, Test: FaintZTF+Noise),
- (iii) training on augmented data but testing on the real faint data (Train: BrightZTF+Noise, Test: FaintZTF),
- (iv) training and testing on augmented data (Train: BrightZTF+Noise, Test: FaintZTF+Noise).

This framework allows us to isolate the effects of noise augmentation on both the training and test sets. Case (ii) evaluates how well a model trained on the real ZTF data performs on noisier data, highlighting its limitations in generalising to fainter flux regimes. Case (iii) examines how augmentation during training improves the model’s ability to classify real faint data. Finally, case (iv) reflects the most realistic use case, as the augmented test data are designed to more closely resemble the ZTF archive of unclassified transients. Figure 10 illustrates these results using the SN Ia recall metric, demonstrating that our model accurately identifies SNe Ia even with fainter, noisier light curves, and that noise augmentation in the training set significantly improves performance. The SN Ia recall increases from 90% to 95% on real data, and from 86% to 96% when tested on fainter, noise-augmented data. The corresponding confusion matrices across different augmentation combinations of BrightZTF and FaintZTF are presented in Fig. D.1 in the Appendix. These results indicate a recall of 96% and a precision of 99% when training on BrightZTF+Noise and testing on FaintZTF+Noise.

To ensure a robust evaluation across the full brightness range, we also performed multiple random splits (RandomZTF) of the data using five different seeds. This approach increases statistical confidence in the reported classification scores by averaging

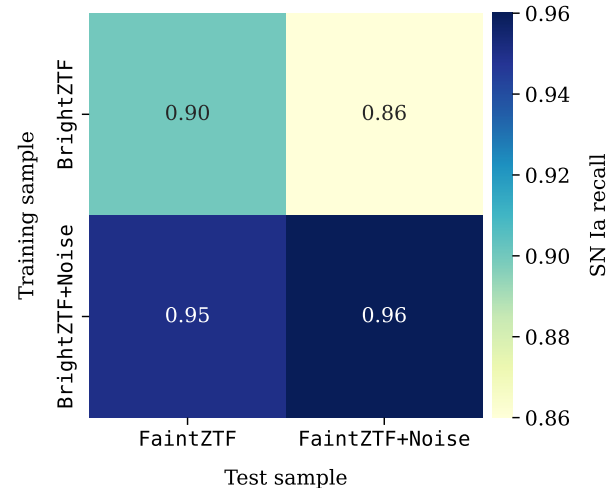


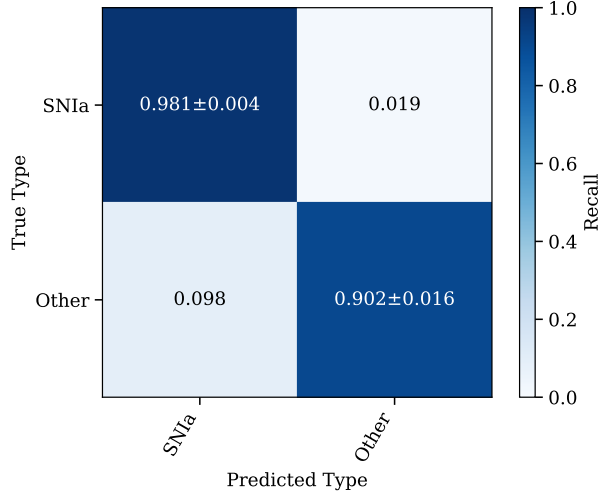
Fig. 10: SN Ia recall for our selected model configuration (bolded in Table 3) across different augmentation combinations of BrightZTF and FaintZTF. The four cases correspond to: (i) training and testing on unaugmented data, (ii) training on unaugmented data and testing on augmented data, (iii) training on augmented data and testing on unaugmented data, and (iv) training and testing on augmented data. The results demonstrate that noise augmentation in the training set improves classification performance on fainter, noisier test samples.

results over different train-test partitions, providing a more reliable estimate of the model’s overall performance. Figure 11 shows the confusion matrices for this configuration, for both the SN Ia binary (panels a and b) and multi-class classifiers (panels c and d). The matrices are normalised by true class totals to show the mean recall and its standard deviation (panels a and c), and by predicted class totals to show the mean precision and its standard deviation (panels b and d).

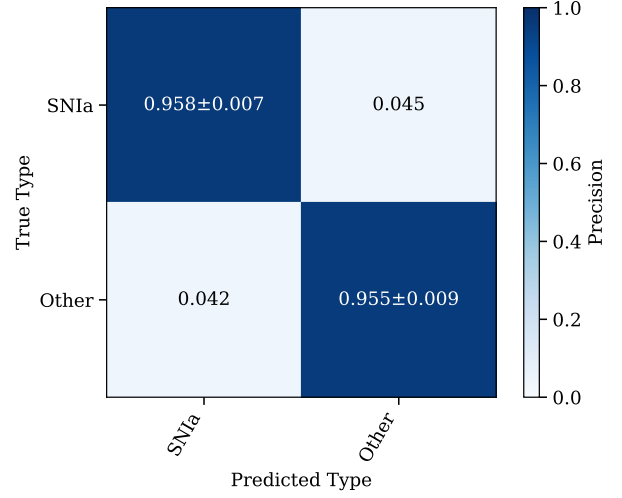
For the SN Ia binary classifier, we note that the SN Ia recall is slightly improved at $(98.1 \pm 0.4\%)$. However, the SN Other recall is slightly lower, with $(90.2 \pm 1.6\%)$ vs. 97% for the BrightZTF+Noise training with FaintZTF+Noise testing. This reduced SN Other recall can be attributed to both the increased difficulty of learning from noisier, more heterogeneous training data and the intrinsic complexity of the SN Other class. The BrightZTF+Noise training sample includes only the brightest 90% of the light curves, which typically have higher SNR photometry. In contrast, the RandomZTF+Noise training set spans a wider brightness range prior to augmentation, including fainter examples of already diverse SN Other classes, with lower SNR and sparser temporal sampling. This can introduce additional noise in the feature space, making it harder for the classifier to learn clear decision boundaries between SN Other types and SNe Ia, causing a decrease in the SN Other recall.

In addition to differences in training data quality, the class composition of the SN Other test sample also varies slightly between the two configurations. The RandomZTF+Noise test sets contain a higher fraction of SNe Ibc (17.8% vs. 14.5%) – a subclass more easily confused with SNe Ia – and a lower fraction of SNe II (62.4% vs. 66.0%), which are generally easier to distinguish. This shift in subclass distribution likely contributes further to the reduced SN Other recall in the RandomZTF+Noise configuration, as a larger fraction of the test set consists of more ambiguous examples.

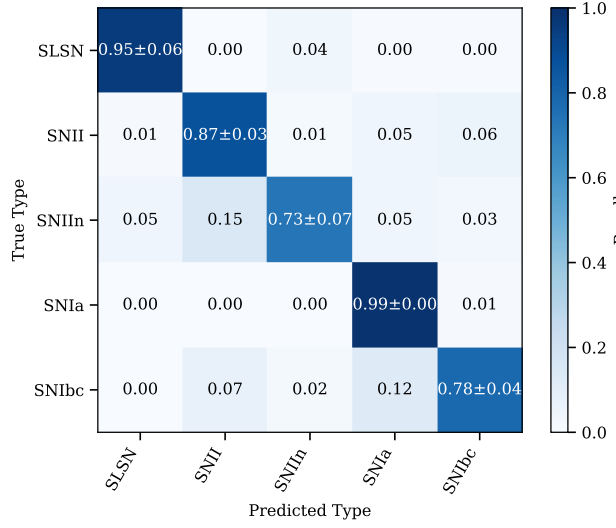
(a) Train: RandomZTF+Noise, Test: RandomZTF+Noise,
SN Ia binary classifier normalised by true class totals.



(b) Train: RandomZTF+Noise, Test: RandomZTF+Noise,
SN Ia binary classifier normalised by predicted class totals.



(c) Train: RandomZTF+Noise, Test: RandomZTF+Noise,
Multi-class classifier normalised by true class totals.



(d) Train: RandomZTF+Noise, Test: RandomZTF+Noise,
Multi-class classifier normalised by predicted class totals.

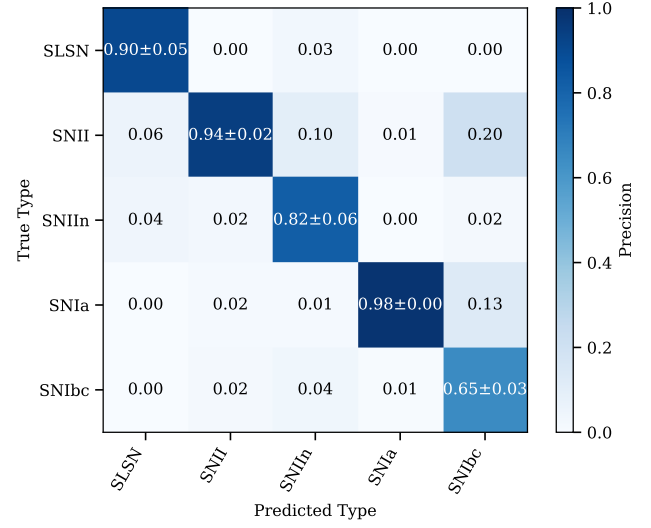


Fig. 11: Confusion matrices averaged over five random train-test sets for both the SN Ia binary (panels a and b) and multi-class classifiers (panels c and d). The matrices are normalised by true class totals to show the mean recall and its standard deviation (panels a and c), and by predicted class totals to show the mean precision and its standard deviation (panels b and d).

For the multi-class classifier, we applied a minimum probability threshold of 0.7 to assign a classification. As a result, 10% of objects remain unclassified. However, this threshold improves both recall and precision across all classes. With this configuration, 95.2% of objects are correctly classified on average across five random seeds. This is comparable with the SN Ia binary classifier, where 95.7% of objects are correctly classified on average.

We can see from the multi-class classifier that the majority of contamination in the SN Ia classification arises from the SN Ib/c class. This is a well-known challenge in photometric classification due to the intrinsic similarities in the light curve shapes and colours of SNe Ia and SNe Ib/c, particularly when observed with limited or noisy data. Both classes can exhibit similar peak magnitudes and decline rates, making them difficult to distinguish solely from photometric features. Such misclassification can significantly contaminate SN Ia cosmological samples and

bias distance estimates. Reducing this contamination might require enhanced feature extraction, such as exploiting the second bump in redder bands, which is unique to SNe Ia. We plan to explore this in future work.

The SN Ia precision is $(95.8 \pm 0.7)\%$ from the SN Ia binary classifier and $(98.1 \pm 0.4)\%$ from the multi-class classifier. While these values are encouraging, they are highly sensitive to the class fractions in the test sample. A more realistic estimate would require simulating the ZTF survey to determine the expected observed distribution of SNe. We leave this for future work.

5.2.1. Dependence on peak apparent magnitude and number of detections

To better understand the limitations of our classifier and the regimes in which it performs most reliably, we investigated how recall varies as a function of two observational parameters: peak

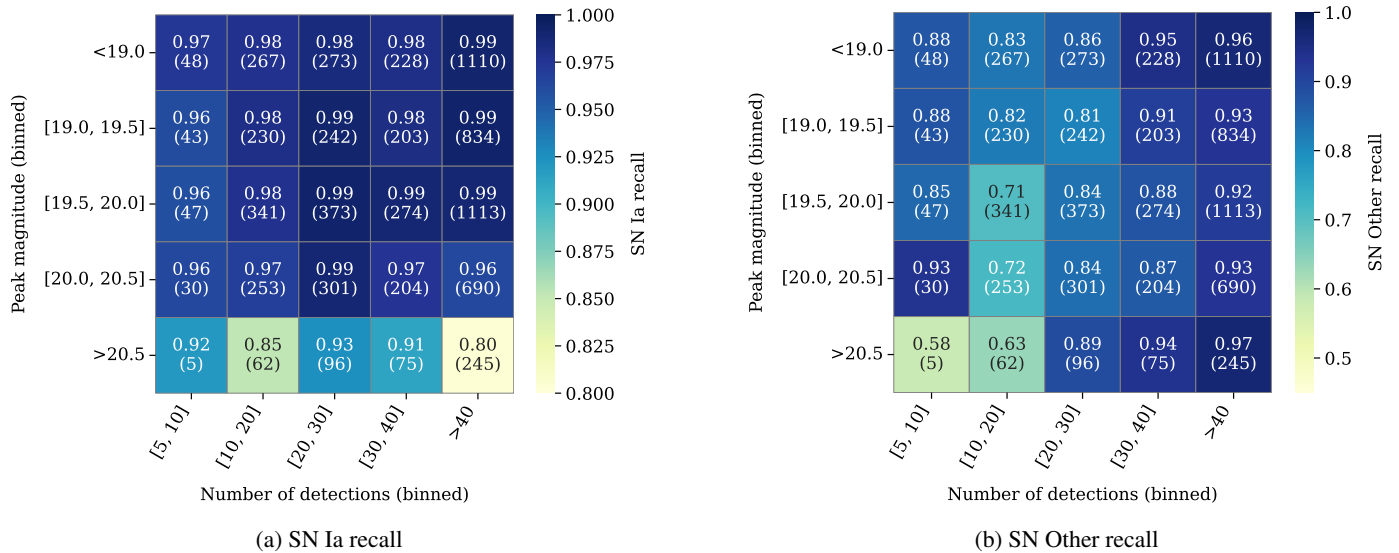


Fig. 12: Heatmaps showing the recall of SN Ia (a) and SN Other (b) as a function of peak apparent magnitude and number of detections, for the RandomZTF+Noise configuration. Each bin shows the mean recall across five random seeds, with the mean number of objects in the bin indicated in parentheses. We include the mean number of objects per bin to provide a sense of the statistical reliability in each region of parameter space. Note that some bins contain a small number of objects, so their reported recall values should be interpreted with caution. SN Ia recall remains high (>98%) for objects brighter than 20 mag and with more than 10 detections, while SN Other recall improves strongly with increasing number of detections and shows weaker dependence on peak apparent magnitude.

apparent magnitude and number of detections. These parameters characterise the quality and completeness of the light curve, with fainter sources and sparsely sampled light curves generally posing greater challenges for classification.

Figure 12 shows the heatmaps of SN Ia and SN Other recall as functions of peak apparent magnitude and number of detections (in any band), for the RandomZTF+Noise configuration. Each bin displays the mean recall, with the mean number of objects in brackets below. For SNe Ia, the classifier performs consistently across a wide range of magnitudes and detection counts. SN Ia recall exceeds 98% for events with a peak apparent magnitude up to 20 and more than 10 detections, and remains above 96% up to magnitude 20.5.

In contrast, the SN Other recall shows a stronger dependence on the number of detections and a weaker dependence on peak apparent magnitude. This indicates that contamination in the SN Ia sample arises primarily from sparsely sampled light curves rather than from faintness alone. The SN Other sample is also likely biased toward intrinsically bright sources (e.g., SLSNe) at the faint end of the magnitude bins. This would explain why the recall remains high for faint objects with many detections, as SLSNe are more easily distinguished from SN Ia than other classes such as SN Ib/c.

5.3. Validation with the ZTF SN Ia DR2 dataset

The ZTF SN Ia DR2 (Rigault et al. 2025) provides a publicly available sample of 3628 spectroscopically classified SNe Ia discovered by ZTF between March 2018 and December 2020. While much of this sample overlaps with the BTS sample used in training, it also includes additional objects not present in BTS, offering an independent test set for our classifiers.

We applied the same quality cuts as for our test samples (see Sect. 4.1), along with a peak apparent magnitude cut at 18.5 to exclude bright objects that could have appeared in the BTS sam-

ple. We also excluded objects that were subtyped as peculiar. Of the 320 remaining SNe Ia, 96% were correctly identified by the BrightZTF+Noise classifier, and 97% were correctly identified by the RandomZTF+Noise classifier. These results are broadly consistent with the SN Ia recall values reported in Sect. 5.2.

Table 4: ZTF SN Ia DR2 sample: photometric classification results. Note that we include misclassifications across all six classifiers, which explains why our correctly classified fraction is lower than the average of 97%.

Classification	Reason	Fraction (#)
Correct	-	94.3% (302)
Incorrect	Bad light curve coverage or bad/failed SALT2 fit	2.8% (9)
	Missing photometry due to baseline corrections	2.2% (7)
	None of the above	0.6% (2)

Notes. Light curves and spectra for the ZTF SN Ia DR2 can be found at ztfcosmo.in2p3.fr/targetlist.

On average, each classifier failed to select about 10 objects as SNe Ia. Across the six classifiers (the BrightZTF+Noise model and five random seeds of the RandomZTF+Noise model), 18 unique objects were excluded from the photometrically identified SN Ia sample. We inspected these objects, and the likely reasons for their misclassification are summarised in Table 4. The majority (2.8%) were already flagged in the DR2 analysis as having poor light curve coverage (e.g., limited early or late-time data) or poor SALT2 fits (typically due to low fit probabilities derived from the χ^2 distribution). Additionally, seven objects (2.2%) were missing a significant number of detections in our forced photometry, particularly in the i - or g -bands, compared to DR2. This is likely due to differences in baseline correction, which can cause detections to be flagged as unreliable

and removed. Only two objects (0.6%) showed no clear reason for misclassification.

5.4. Discussion of contamination from peculiar subtypes

We excluded both peculiar and uncommon subtypes from model training and testing due to insufficient sample sizes to effectively model their behaviour, and to avoid biasing the main classes. However, following the approach of [de Soto et al. \(2024\)](#), we tested the classifier on these excluded types to examine how they would be classified in practice. The data were processed using the same quality cuts as our test samples (Sect. 4.1). We applied both the BrightZTF+Noise binary and multi-class classifiers to the peculiar test set without augmentation. Table 5 shows the fraction of each subtype classified as SN Ia and the fraction misclassified. The total number of objects in each class is shown in parentheses in the left-hand column. Table 6 expands on this by presenting the predicted class fractions for each peculiar subtype from the multi-class classifier.

Table 5: Peculiar objects: SN Ia classification and misclassification rate.

True type (#)	SN Ia classification (%)		Misclassified (%)	
	Binary	Multi	Binary	Multi
Ia-pec (202)	48.0	39.1	52.0	60.9
II-pec (134)	8.2	4.5	8.2	67.2
Ib/c-pec (34)	61.8	52.9	61.8	88.2
TDE (33)	6.1	6.1	6.1	-

Notes. The fractions shown are relative to the true class totals. For the binary classifier, a misclassification occurs when a non-Ia-peculiar object is classified as an SN Ia. For the multi-class classifier, a misclassification rate is not possible for TDEs since we do not include them in the model training.

Table 6: Peculiar objects: multi-class classifier results.

True type (#)	Predicted class (%)				
	SN Ia	SN II	SN IIn	SN Ibc	SLSN
Ia-pec (202)	39.1	4.5	6.9	47.0	2.4
II-pec (134)	4.5	32.8	0.0	62.7	0.0
Ib/c-pec (34)	52.9	26.5	8.8	11.8	0.0
TDE (33)	6.1	9.1	36.3	3.0	45.4

Notes. The fractions shown are relative to the true class totals.

For SN Ia cosmology, we aim to exclude peculiar SN types from our cosmological sample, which is why our training and test sets only included SNe Ia, SNe Ia-norm, and SNe Ia-91T. However, it is evident that some peculiar subtypes are still classified as SN Ia by our model. Examining the SN Ia-pec classifications, we find that most SN Iax and all SN Ia-CSM are correctly excluded from the SN Ia class – likely because their light curves deviate more significantly from the SALT2 model, with Ia-CSM objects often showing bumps or plateaus from circumstellar interaction. In contrast, large fractions of Ia-91bg, Ia-03fg, Ia-00cx, and Ia-pec are still classified as SN Ia. To mitigate contamination from these subtypes in a cosmological sample, we could either train a model including these types (potentially using simulations to increase the training sample) or apply additional selection cuts to remove them.

There is significant SN Ia contamination in the Ib/c-pec class, primarily due to the Ibn subclass. SN Ibn light curves

can exhibit rapid rises and declines that resemble those of some SNe Ia, making them difficult to distinguish photometrically without spectroscopic data. As with the Ia-pec subtypes, this contamination can be mitigated by applying additional selection cuts to the cosmological sample. SNe Ibn are also sometimes misclassified as SNe II because their early blue colours, caused by helium-rich circumstellar interaction, differ significantly from the redder colours of typical SNe Ib/c and resemble the early phases of SNe II.

The subtype II-pec, which is mostly comprised of SNe IIb, is mostly classified as SN Ib/c. This is expected, since SNe IIb share similar photometric properties with SNe Ib/c due to their partially stripped hydrogen envelopes, resulting in similar light curve features such as relatively fast declines compared to SNe II. Previous studies have shown that the light curve properties of SNe IIb are observationally distinct from those of SNe II ([Pessi et al. 2019](#)). Based on this, we propose including SNe IIb in future classifiers either as part of the SN Ib/c class or as a separate class.

In addition, TDEs are mostly classified as SLSNe or SNe IIn, likely due to their high luminosity and long-duration light curves. In future work, we aim to include TDEs as a separate class.

5.5. Application in supernova cosmology

We have demonstrated that our classifier achieves high accuracy in identifying SNe Ia, with an efficiency exceeding 98% for objects brighter than a peak apparent magnitude of 20.5 and having more than 20 detections, when evaluated on real observational data. However, before applying this classifier to the full ZTF sample of unclassified transients, it is essential to simulate the survey realistically. This simulation will allow us to estimate the expected number of SNe Ia in our sample, quantify contamination from other SN types, estimate selection biases, and assess classifier performance under different survey conditions. This is similar to the approach of the DES collaboration (e.g., [Vincenzi et al. 2021, 2023](#)).

When applied to the full ZTF transient sample, our classifier will enable the construction of a large, photometrically classified SN Ia sample. This dataset will be valuable not only for cosmological analyses, but also for improving the standardisation of SNe Ia through environmental studies. The Bright Transient Survey in ZTF has recorded approximately 8,000 spectroscopically confirmed SNe Ia up to a magnitude of 19 by the end of 2024. However, as was shown in the ZTF SN Ia DR2 ([Rigault et al. 2025](#)), many additional SNe Ia are present in the ZTF sample that were not included in BTS, estimated to number around 10,000. Assuming the number of SNe Ia roughly doubles with every 0.5 mag of additional depth, we could expect up to 40,000 photometrically classified SNe Ia up to a magnitude of 21. A key limiting factor remains the availability of redshift information, which is typically obtained from spectroscopic host galaxy surveys. Efforts such as the MOST Hosts Survey ([Soumagnac et al. 2024](#)) aim to address this by building a comprehensive spectroscopic redshift catalogue for the host galaxies of known transients.

In this work, we prioritised maximising SN Ia recall to select the best classifier, motivated by previous studies showing that the BBC approach to cosmology with photometric classification can correct for non-Ia contamination (e.g., [Vincenzi et al. 2024](#)). However, [Malz et al. \(2025\)](#) demonstrated that cosmological constraints are sensitive not only to the contamination rate but also to the class of the contaminating population. Traditional classification metrics like recall and precision do not consider

the latter. Instead, cosmology-based metrics, such as assessing the cosmological parameter constraints, are more appropriate. We plan to explore these metrics in future studies.

An alternative strategy is proposed by [Boone \(2021\)](#), in which the same ParSNIP latent-space model is used to jointly classify transients and estimate their distances. Rather than selecting a pure SN Ia sample, this approach derives distance estimates for all transient types compatible with a given light curve, weighted by their likelihood. This is done by marginalising over the latent-space posterior from the ParSNIP model (i.e., the class probability distribution). The goal is to reduce biases introduced when non-Ia contaminants are assigned distances using models trained on SNe Ia. Implementing this requires fitting a distance modulus zeropoint model across the full population, including classes with broad luminosity distributions. While promising, this method presents challenges, particularly in accurately modelling the zeropoint and quantifying the light curve modelling uncertainties at the level required for precision cosmology.

5.6. The NoiZTF survey: application in real-time classification

Although our primary motivation for developing this classifier was SN Ia cosmology, it is also effective for real-time transient classification and prioritising candidates for spectroscopic follow-up in ongoing surveys. The relatively nearby ZTF sample provides a unique opportunity to validate our photometric classifications, and we leveraged this by conducting a live follow-up program – denoted the NoiZTF survey, as in "noisy ZTF" – as part of the ePESSTO+ collaboration ([Smartt et al. 2015](#)).

The ePESSTO+ survey operates on the 3.5-metre NTT at La Silla, using the EFOSC2 instrument to spectroscopically classify transients. We submitted SN-like targets for spectroscopic classification across multiple observing nights between July and November 2024. For this study, we used an earlier version of our classifier that did not include SN IIn as a separate class; therefore, the performance may not be directly comparable to the results presented in Sect. 5.2.

Candidates were selected using the AMPEL alert broker ([Nordin et al. 2019](#)). We queried the AMPEL API for ZTF alerts that passed basic SN-like criteria from the previous three days. The filtering criteria included a point spread function (PSF) apparent magnitude of greater than 18; greater than six previous detections but fewer than 50; a real bogus (RB) value of greater than 0.2; and a positive flux value. Probable stars were rejected based on matches to the Pan-STARRS PS1 and Gaia DR2 catalogues. To get estimates for the redshift of the transient, we crossmatched to various galaxy catalogues that were available within AMPEL⁷. The redshift catalogues that we queried are as follows: Sloan Digital Sky Survey (SDSS) DR10 ([Brescia et al. 2015](#)); NASA/IPAC Extragalactic Database (NED⁸), accessed through the catsHTM tool ([Soumagnac & Ofek 2018](#)); Galaxy List for the Advanced Detector Era (GLADE) v2.3 ([Dálya et al. 2018](#)); WISExSCOS Photometric Redshift Catalogue (WISExSCOS-PZ; [Bilicki et al. 2016](#)); 2MASS Photometric Redshift catalogue (2MPZ; [Bilicki et al. 2014](#)); Legacy Survey (LS) DR8 ([Duncan 2022](#)); Pan-STARRS1 Source Types and Redshifts with Machine Learning (PS1-STRM; [Beck et al. 2021](#)).

To exclude old transients or highly variable extragalactic sources (e.g., AGN), we required fewer than 50 detections and a light curve duration of less than 90 days. The multi-class classifier with a probability threshold of 0.7 was applied to the re-

maining candidate transients. For each candidate, we computed its visibility from La Silla, defined as the number of hours it was observable at an airmass below 2.5, requiring a minimum visibility of one hour. We then assigned priorities to the candidates based on a points-based system, with points awarded for meeting the following criteria:

1. The predicted class was rarer (i.e., not SN Ia),
2. The object had already peaked (noting this was occasionally inaccurate for sources with re-brightenings or bumps),
3. The most recent detection was fainter than 19 mag,
4. The peak apparent magnitude was fainter than 19 mag,
5. The catalogue-matched redshift was $z < 0.4$ (due to less reliable photometric redshifts at higher z).

Candidates were then ranked by total priority score, redshift catalogue reliability, and visibility. While we aimed to select the highest-ranked targets for classification, observational constraints such as scheduling or poor weather at La Silla often required selecting lower-priority (generally brighter) objects.

Table E.1 in the Appendix lists the 40 sources that received spectroscopic classifications, along with their predicted class, true class, and the number of detections at the time of photometric classification. We also include objects that were submitted to the ePESSTO+ marshall to be observed, but were classified by other groups first and reported on the Transient Name Server (TNS)⁹. Every candidate submitted was classified as an SN or TDE, except for one case in which the spectrum was too noisy to allow classification. This demonstrates that combining alert brokers with photometric classifiers enables effective prioritisation of real transients for spectroscopic follow-up.

Although the NoiZTF survey was relatively limited in scope (e.g., we were not able to test any SN Ib/c predictions), it produced several informative results. Of the 19 true SNe Ia, 17 were correctly classified, giving an SN Ia recall of 89%. The two misclassified SNe Ia were affected by inaccurate high photometric redshifts ($z > 0.4$) from catalogue crossmatches, which likely led to incorrect SLSN classifications. Four non-Ia objects (SNe II or SNe Ib/c) were falsely classified as SNe Ia, resulting in an SN Ia precision of 81%. The misclassifications were primarily caused by either sparse light curves – with fewer than 10 detections – or, in the case of SN 2024seh, an unusually high luminosity ($M \sim -19.7$) that is atypical for SNe II.

For the spectroscopically classified SNe II, 7 out of 11 were correctly identified, resulting in an SN II recall of 64%. Misclassifications were again likely caused by inaccurate high photometric redshifts, low detection counts, or intrinsic brightness anomalies (e.g., SN 2024seh). Of the 8 objects predicted by the classifier to be SNe II, 7 were indeed SNe II, giving an SN II precision of 88%.

The classifier performed particularly well for rare classes such as SLSNe. All four spectroscopically confirmed SLSNe (including one SLSN-IIn) were correctly identified by the classifier (100% SLSN recall). However, precision was affected by the same redshift errors – several lower-luminosity objects were incorrectly classified as SLSNe due to inaccurate redshift estimates. One TDE (TDE 2024mvz) was misclassified as an SLSN, which is an expected result given that TDEs were not represented among the classifier's training classes and TDEs are also known to have high luminosities. Three additional SLSN candidates (SN 2024qef, SN 2024uhx, and AT 2024syj) lacked conclusive spectroscopic classifications due to noisy or featureless spectra. SN 2024qef was initially classified as 'SN' due to

⁷ ampel.zeuthen.desy.de/api/catalogmatch/docs

⁸ ned.ipac.caltech.edu

⁹ wis-tns.org

its blue, featureless spectrum. However, later-phase spectra obtained through a follow-up program with ePESSTO+ were consistent with an SN Ib-pec or Ic-BL classification at $z \sim 0.28$. This redshift implies a peak absolute magnitude of $M < -21$, consistent with an SLSN-I interpretation. An example spectrum and the corresponding spectral template fits are shown in Fig. E.1. AT 2024syj exhibited a light curve lasting over 100 days, consistent with SLSN behaviour. Therefore, a total of 7 out of the 11 objects predicted as SLSNe were either confirmed SLSNe, a TDE, or likely SLSNe, resulting in an effective precision of 64%.

Across the entire sample – excluding objects with inconclusive classifications or those not recognised by the classifier (e.g., TDEs) – we correctly predicted the class for 78% of the sources. The median number of detections at the time of photometric classification was nine, highlighting the robustness of our method even with limited data. With the latest version of our classifier, this approach provides reliable and efficient target prioritisation for spectroscopic follow-up. This program was a valuable prototype for the Vera C. Rubin Observatory’s LSST, where photometric classification will be essential due to the survey’s depth and data volume. Using real data, we have demonstrated that photometric classification enables efficient selection of promising transient candidates for spectroscopic confirmation, which is vital for the future of time-domain astronomy in LSST.

LSST will provide multi-band photometry (in *ugrizy*), which can significantly aid photometric classification by providing more colour information. This is particularly helpful for distinguishing between SN subtypes with similar light curve shapes but different colours, such as SNe Ia and SNe Ib/c. However, LSST’s lower cadence compared to ZTF may limit light curve sampling, posing challenges for accurate classification. In future work, our method will be adapted to LSST photometry, and performance may be further improved by combining our classifier with contextual models that incorporate host galaxy information or are specialised in identifying rarer classes, such as TDEs. A hybrid framework that combines multiple classifiers will likely be essential to enable reliable large-scale classification in the LSST era.

6. Conclusions

In this work, we presented a feature-based photometric classifier for SNe detected by ZTF, with the primary goal of constructing a photometric SN Ia sample for cosmological analyses. Our approach utilises the autoencoder architecture from the ParSNIP model (Boone 2021) to capture the intrinsic diversity of SN light curves. We trained the model on the ZTF SN sample, incorporating a realistic noise augmentation procedure that simulates the flux uncertainties of fainter sources. This enables the model to generalise to noisier, higher-redshift populations. Light curve features were used to train a gradient-boosted decision tree classifier, implemented in both binary (SN Ia vs. non-Ia) and multi-class configurations. We validated our classifier on independent, fainter ZTF data with and without noise augmentation. To evaluate real-time performance, we also applied our classifier to live ZTF alerts and conducted a spectroscopic classification survey within the ePESSTO+ collaboration.

The conclusions of our analysis are as follows:

1. Noise augmentation significantly improves classification performance, particularly for fainter sources. We showed that

SN Ia recall increases from 90% to 95% on real data, and from 86% to 96% on fainter, noise-augmented data.

2. Our binary classifier achieves an SN Ia recall of $(98.1 \pm 0.4)\%$, averaged across five train-test splits. The classifier performs consistently across a wide range of magnitudes and detection counts: SN Ia recall exceeds 98% for events with a peak apparent magnitude up to 20 and more than 10 detections, and remains above 96% up to magnitude 20.5.
3. Overall, 95% of sources were correctly classified in both binary and multi-class modes.
4. In our live classification survey, we correctly identified the class for 78% of the targets, including rare events such as SLSNe, despite a median of only nine detections per object. We measured an SN Ia recall of 89% and a precision of 81%. All four spectroscopically confirmed SLSNe were correctly identified by the classifier (100% SLSN recall). Of the 11 objects predicted as SLSNe, 7 were either confirmed SLSNe, a TDE, or likely SLSNe, resulting in an effective precision of 64%. This is notable given that the classification relied on photometric redshift catalogues to estimate the transient redshift.

Our classifier performs efficiently on real ZTF data, including faint and noisy light curves. When applied to the full ZTF transient sample, our classifier will enable the construction of a large photometrically classified SN Ia sample for cosmology. Our next steps include simulating the ZTF survey realistically. This simulation will allow us to estimate the expected number of SNe Ia in our photometric sample, quantify contamination from other SN types, estimate selection biases, and assess classifier performance under survey conditions. Additionally, our methodology offers an effective tool for real-time target prioritisation for spectroscopic follow-up, which will be essential for future large-scale surveys such as LSST.

7. Data availability

ZTF light curve data is publicly available at ztf.caltech.edu/ztf-public-releases.html. A repository that contains the code used to generate the training and test samples, along with the model files for feature generation from any light curve, and the classifier files for running your own classifications can be found here: github.com/aotownsend/noiztf/tree/v1.0.0.

Acknowledgements. Based on observations obtained with the Samuel Oschin Telescope 48-inch and the 60-inch Telescope at the Palomar Observatory as part of the Zwicky Transient Facility project. ZTF is supported by the National Science Foundation under Grants No. AST-1440341, AST-2034437, and currently Award #2407588. ZTF receives additional funding from the ZTF partnership. Current members include Caltech, USA; Caltech/IPAC, USA; University of Maryland, USA; University of California, Berkeley, USA; University of Wisconsin at Milwaukee, USA; Cornell University, USA; Drexel University, USA; University of North Carolina at Chapel Hill, USA; Institute of Science and Technology, Austria; National Central University, Taiwan, and OKC, University of Stockholm, Sweden. Operations are conducted by Caltech’s Optical Observatory (COO), Caltech/IPAC, and the University of Washington at Seattle, USA. The ZTF forced-photometry service was funded under the Heising-Simons Foundation grant #12540303 (PI: Graham). The Gordon and Betty Moore Foundation, through both the Data-Driven Investigator Program and a dedicated grant, provided critical funding for SkyPortal.

Based on observations collected at the European Organisation for Astronomical Research in the Southern Hemisphere, Chile, as part of ePESSTO+ (the advanced Public ESO Spectroscopic Survey for Transient Objects Survey – PI: Inserra), under ESO program ID 112.25JQ.

K.M., T.E.M.B. and U.B. acknowledge funding from Horizon Europe ERC grant no. 101125877. T.-W.C. acknowledges the financial support from the Yushan Fellow Program by the Ministry of Education, Taiwan (MOE-111-YSFMS-0008-001-P1) and the National Science and Technology Council, Taiwan (NSTC grant 114-2112-M-008-021-MY3). Y.-L.K. was supported by the

Lee Wonchul Fellowship, funded through the BK21 Fostering Outstanding Universities for Research (FOUR) Program (grant No. 4120200513819) and the National Research Foundation of Korea to the Center for Galaxy Evolution Research (RS-2022-NR070872, RS-2022-NR070525). S.Y. acknowledges the funding from the National Natural Science Foundation of China under grant No. 12303046, and the Startup Research Fund of Henan Academy of Sciences No.242041217. C.P.G. acknowledges financial support from the Secretary of Universities and Research (Government of Catalonia) and by the Horizon 2020 Research and Innovation Programme of the European Union under the Marie Skłodowska-Curie and the Beatriu de Pinós 2021 BP 00168 programme, from the Spanish Ministerio de Ciencia e Innovación (MCIN) and the Agencia Estatal de Investigación (AEI) 10.13039/501100011033 under the PID2023-151307NB-I00 SNNEXT project, from Centro Superior de Investigaciones Científicas (CSIC) under the PIE project 20215AT016 and the program Unidad de Excelencia María de Maeztu CEX2020-001058-M, and from the Departament de Recerca i Universitats de la Generalitat de Catalunya through the 2021-SGR-01270 grant. L.G. acknowledges financial support from AGAUR, CSIC, MCIN and AEI 10.13039/501100011033 under projects PID2023-151307NB-I00, PIE 20215AT016, CEX2020-001058-M, ILINK23001, COOPB2304, and 2021-SGR-01270.

References

Abbott, T. M. C., Allam, S., Andersen, P., et al. 2019, *ApJ*, 872, L30

Abdelhadi, B. & Rubin, D. 2024, *PASP*, 136, 124504

Aleo, P. D., Malanchev, K., Sharief, S., et al. 2023, *ApJS*, 266, 9

Alves, C. S., Peiris, H. V., Lochner, M., et al. 2022, *ApJS*, 258, 23

Angus, C. 2024, Transient Name Server Classification Report, 2024-4675, 1

Barbary, K., Bailey, S., Barentsen, G., et al. 2022, SNCosmo

Beck, R., Szapudi, I., Flewelling, H., et al. 2021, *MNRAS*, 500, 1633

Bellm, E. C., Kulkarni, S. R., Barlow, T., et al. 2019a, *PASP*, 131, 068003

Bellm, E. C., Kulkarni, S. R., Graham, M. J., et al. 2019b, *PASP*, 131, 018002

Betoule, M., Kessler, R., Guy, J., et al. 2014, *A&A*, 568, A22

Bilicki, M., Jarrett, T. H., Peacock, J. A., Cluver, M. E., & Steward, L. 2014, *ApJS*, 210, 9

Bilicki, M., Peacock, J. A., Jarrett, T. H., et al. 2016, *ApJS*, 225, 5

Blagorodnova, N., Jones, D., Lavers, A. L. C., et al. 2024, Transient Name Server Classification Report, 2024-4731, 1

Blagorodnova, N., Neill, J. D., Walters, R., et al. 2018, *PASP*, 130, 035003

Blondin, S. & Tonry, J. L. 2007, *ApJ*, 666, 1024

Boone, K. 2019, *AJ*, 158, 257

Boone, K. 2021, *AJ*, 162, 275

Brescia, M., Cavuoti, S., & Longo, G. 2015, *MNRAS*, 450, 3893

Brout, D., Scolnic, D., Popovic, B., et al. 2022, *ApJ*, 938, 110

Burgaz, U., Maguire, K., Dimitriadis, G., et al. 2025, *A&A*, 694, A9

Campbell, H., D'Andrea, C. B., Nichol, R. C., et al. 2013, *ApJ*, 763, 88

Carrick, J. E., Hook, I. M., Swann, E., et al. 2021, *MNRAS*, 508, 1

Chen, Z. H., Yan, L., Kangas, T., et al. 2023, *ApJ*, 943, 41

Coughlin, M. W., Bloom, J. S., Nir, G., et al. 2023, *ApJS*, 267, 31

Covarrubias, S., Chu, M., & Fremling, C. 2024, Transient Name Server Classification Report, 2024-4958, 1

Dálya, G., Galgóczki, G., Dobos, L., et al. 2018, *MNRAS*, 479, 2374

de Soto, K. M., Villar, V. A., Berger, E., et al. 2024, *ApJ*, 974, 169

Dekany, R., Smith, R. M., Riddle, R., et al. 2020, *PASP*, 132, 038001

DES Collaboration, Abbott, T. M. C., Acevedo, M., et al. 2024, *ApJ*, 973, L14

Dgany, Y., Moore, T., Mohsen, S., Bruch, R. J., & Zimmerman, E. A. 2024, Transient Name Server Classification Report, 2024-3143, 1

Dimitriadis, G., Burgaz, U., Deckers, M., et al. 2025, *A&A*, 694, A10

Dimitriadis, G., Milligan, A., Ghendrih, M., et al. 2024, Transient Name Server AstroNote, 281, 1

Duarte, J., Gonzalez-Gaitan, S., Gutierrez, C., & Bruch, R. J. 2024a, Transient Name Server Classification Report, 2024-2386, 1

Duarte, J., Gonzalez-Gaitan, S., Gutierrez, C., & Bruch, R. J. 2024b, Transient Name Server Classification Report, 2024-2424, 1

Duncan, K. J. 2022, *MNRAS*, 512, 3662

Förster, F., Cabrera-Vives, G., Castillo-Navarrete, E., et al. 2021, *AJ*, 161, 242

Fremling, C., Covarrubias, S., & Chu, M. 2024, Transient Name Server Classification Report, 2024-4729, 1

Fremling, C., Hall, X. J., Coughlin, M. W., et al. 2021, *ApJ*, 917, L2

Fremling, C., Miller, A. A., Sharma, Y., et al. 2020, *ApJ*, 895, 32

Gagliano, A. 2024, Transient Name Server Classification Report, 2024-4932, 1

Gagliano, A., Contardo, G., Foreman-Mackey, D., Malz, A. I., & Aleo, P. D. 2023, *ApJ*, 954, 6

Gagliano, A., Narayan, G., Engel, A., Carrasco Kind, M., & LSST Dark Energy Science Collaboration. 2021, *ApJ*, 908, 170

Gomez, S., Berger, E., Blanchard, P. K., et al. 2020, *ApJ*, 904, 74

Gonzalez-Banuelos, M., Alburai, A., Kopsacheili, M., Taubenberger, S., & Yaron, O. 2024a, Transient Name Server Classification Report, 2024-2189, 1

Gonzalez-Banuelos, M., Alburai, A., Kopsacheili, M., Taubenberger, S., & Zimmerman, E. A. 2024b, Transient Name Server Classification Report, 2024-2256, 1

Gonzalez-Gaitan, S., Duarte, J., Gutierrez, C., & Bruch, R. J. 2024, Transient Name Server Classification Report, 2024-2404, 1

Graham, M. J., Kulkarni, S. R., Bellm, E. C., et al. 2019, *PASP*, 131, 078001

Guy, J., Astier, P., Baumont, S., et al. 2007, *A&A*, 466, 11

Hložek, R., Malz, A. I., Ponder, K. A., et al. 2023, *ApJS*, 267, 25

Hložek, R., Kunz, M., Bassett, B., et al. 2012, *ApJ*, 752, 79

Hogg, D. W., Baldry, I. K., Blanton, M. R., & Eisenstein, D. J. 2002, arXiv e-prints, astro

Hu, Y., Tsalapatas, K., Pessi, P. J., et al. 2024, Transient Name Server Classification Report, 2024-4425, 1

Ivezić, Ž., Kahn, S. M., Tyson, J. A., et al. 2019, *ApJ*, 873, 111

Jones, D. O., Scolnic, D. M., Riess, A. G., et al. 2018, *ApJ*, 857, 51

Kangas, T., Yan, L., Schulze, S., et al. 2022, *MNRAS*, 516, 1193

Ke, G., Meng, Q., Finley, T., et al. 2017, in Proceedings of the 31st International Conference on Neural Information Processing Systems, NIPS'17 (Red Hook, NY, USA: Curran Associates Inc.), 3149–3157

Kennamer, N., Ishida, E. E. O., Gonzalez-Gaitan, S., et al. 2020, arXiv e-prints, arXiv:2010.05941

Kessler, R., Bassett, B., Belov, P., et al. 2010, *PASP*, 122, 1415

Kessler, R. & Scolnic, D. 2017, *ApJ*, 836, 56

Kim, Y. L., Rigault, M., Neill, J. D., et al. 2022, *PASP*, 134, 024505

Kingma, D. P. & Ba, J. 2014, arXiv preprint arXiv:1412.6980

Kingma, D. P. & Welling, M. 2013, arXiv e-prints, arXiv:1312.6114

Kisley, M., Qin, Y.-J., Zabludoff, A., Barnard, K., & Ko, C.-L. 2023, *ApJ*, 942, 29

Kunz, M., Hložek, R., Bassett, B. A., et al. 2013, in *Astrostatistical Challenges for the New Astronomy*, ed. J. M. Hilbe, 1013

Leoni, M., Ishida, E. E. O., Peloton, J., & Möller, A. 2022, *A&A*, 663, A13

Lochner, M., McEwen, J. D., Peiris, H. V., Lahav, O., & Winter, M. K. 2016, *ApJS*, 225, 31

Malz, A. I., Dai, M., Ponder, K. A., et al. 2025, *A&A*, 694, A130

Masci, F. J., Laher, R. R., Rusholme, B., et al. 2023, arXiv e-prints, arXiv:2305.16279

Masci, F. J., Laher, R. R., Rusholme, B., et al. 2019, *PASP*, 131, 018003

Mehta, D., Valenti, S., Retamal, N. M., et al. 2024, Transient Name Server Classification Report, 2024-3325, 1

Miranda, N., Freytag, J. C., Nordin, J., et al. 2022, *A&A*, 665, A99

Mohsen, S., Katz, T., Moore, T., Bruch, R. J., & Yaron, O. 2024, Transient Name Server Classification Report, 2024-3256, 1

Möller, A. & de Boissière, T. 2020, *MNRAS*, 491, 4277

Möller, A., Smith, M., Sako, M., et al. 2022, *MNRAS*, 514, 5159

Moore, T., Keinan, I., Shitrit, N., et al. 2024, Transient Name Server Classification Report, 2024-3215, 1

Muthukrishna, D., Narayan, G., Mandel, K. S., Biswas, R., & Hložek, R. 2019, *PASP*, 131, 118002

Narayan, G. & ELAsTiCC Team. 2023, in *AAS Meeting Abstracts*, Vol. 241, 117.01

Nordin, J., Brinnel, V., van Santen, J., et al. 2019, *A&A*, 631, A147

Nordin, J., Brinnel, V., van Santen, J., Reusch, S., & Kowalski, M. 2025, *A&A*, 698, A13

Oke, J. B. & Sandage, A. 1968, *ApJ*, 154, 21

Pasquet, J., Pasquet, J., Chaumont, M., & Fouchez, D. 2019, *A&A*, 627, A21

Patterson, M. T., Bellm, E. C., Rusholme, B., et al. 2019, *PASP*, 131, 018001

Perley, D. A., Fremling, C., Sollerman, J., et al. 2020, *ApJ*, 904, 35

Perlmutter, S., Aldering, G., Goldhaber, G., et al. 1999, *ApJ*, 517, 565

Pessi, P. J., Folatelli, G., Anderson, J. P., et al. 2019, *MNRAS*, 488, 4239

Pessi, P. J., Hu, Y., Tsalapatas, K., et al. 2024a, Transient Name Server Classification Report, 2024-4388, 1

Pessi, P. J., Lunnan, R., Sollerman, J., et al. 2025, *A&A*, 695, A142

Pessi, P. J., Tsalapatas, K., Hu, Y., et al. 2024b, Transient Name Server Classification Report, 2024-4356, 1

Phillips, M. M. 1993, *ApJ*, 413, L105

Pimentel, Ó., Estévez, P. A., & Förster, F. 2023, *AJ*, 165, 18

Planck Collaboration, Aghanim, N., Akrami, Y., et al. 2020, *A&A*, 641, A6

Popovic, B., Scolnic, D., Vincenzi, M., et al. 2024, *MNRAS*, 529, 2100

Qu, H., Sako, M., Möller, A., & Doux, C. 2021, *AJ*, 162, 67

Ramirez, M., Ayala, B., Dastidar, R., Kumar, A., & Yaron, O. 2024a, Transient Name Server Classification Report, 2024-3366, 1

Ramirez, M., Ayala, B., Dastidar, R., Kumar, A., & Yaron, O. 2024b, Transient Name Server Classification Report, 2024-3408, 1

Rasmussen, C. E. & Williams, C. K. I. 2006, *Gaussian Processes for Machine Learning* (The MIT Press)

Rehmetulla, N., Miller, A. A., Jegou Du Laz, T., et al. 2024, *ApJ*, 972, 7

Revsbech, E. A., Trotta, R., & van Dyk, D. A. 2018, *MNRAS*, 473, 3969

Richards, J. W., Homrighausen, D., Freeman, P. E., Schafer, C. M., & Poznanski, D. 2012, MNRAS, 419, 1121

Riess, A. G., Filippenko, A. V., Challis, P., et al. 1998, AJ, 116, 1009

Riess, A. G., Press, W. H., & Kirshner, R. P. 1996, ApJ, 473, 88

Rigault, M., Neill, J. D., Blagorodnova, N., et al. 2019, A&A, 627, A115

Rigault, M., Smith, M., Goobar, A., et al. 2025, A&A, 694, A1

Sako, M., Bassett, B., Connolly, B., et al. 2011, ApJ, 738, 162

Shah, V. G., Gagliano, A., Malanchev, K., Narayan, G., & The LSST Dark Energy Science Collaboration. 2025, arXiv e-prints, arXiv:2501.01496

Sharma, Y., Mahabal, A. A., Sollerman, J., et al. 2025, PASP, 137, 034507

Sheng, X., Nicholl, M., Smith, K. W., et al. 2024, MNRAS, 531, 2474

Shitrit, N., Mohsen, S., Keinan, I., et al. 2024a, Transient Name Server Classification Report, 2024-3255, 1

Shitrit, N., Moore, T., Faris, S., Bruch, R. J., & Zimmerman, E. A. 2024b, Transient Name Server Classification Report, 2024-3120, 1

Smartt, S. J., Valenti, S., Fraser, M., et al. 2015, A&A, 579, A40

Sollerman, J., Covarrubias, S., Chu, M., & Fremling, C. 2024a, Transient Name Server Classification Report, 2024-4704, 1

Sollerman, J., Covarrubias, S., Chu, M., & Fremling, C. 2024b, Transient Name Server Classification Report, 2024-4840, 1

Soumagnac, M. T., Nugent, P., Knop, R. A., et al. 2024, ApJS, 275, 22

Soumagnac, M. T. & Ofek, E. O. 2018, PASP, 130, 075002

Stein, R., Mahabal, A., Reusch, S., et al. 2024, ApJ, 965, L14

Townsend, A., Gutiérrez, C., Aryan, A., et al. 2024a, Transient Name Server Classification Report, 2024-4592, 1

Townsend, A., Gutiérrez, C., Aryan, A., et al. 2024b, Transient Name Server Classification Report, 2024-4702, 1

Tripp, R. 1998, A&A, 331, 815

Tsalapatas, K., Hu, Y., Pessi, P. J., et al. 2024, Transient Name Server Classification Report, 2024-4471, 1

van der Walt, S. J., Crellin-Quick, A., & Bloom, J. S. 2019, Journal of Open Source Software, 4, 1247

Villar, V. A., Berger, E., Miller, G., et al. 2019, ApJ, 884, 83

Villar, V. A., Hosseinzadeh, G., Berger, E., et al. 2020, ApJ, 905, 94

Vincenzi, M., Brout, D., Armstrong, P., et al. 2024, ApJ, 975, 86

Vincenzi, M., Sullivan, M., Graur, O., et al. 2021, MNRAS, 505, 2819

Vincenzi, M., Sullivan, M., Möller, A., et al. 2023, MNRAS, 518, 1106

Zhang, G., Helfer, T., Gagliano, A. T., Mishra-Sharma, S., & Ashley Villar, V. 2024a, Machine Learning: Science and Technology, 5, 045069

Zhang, L.-W., Wang, Z.-Y., Liu, D.-Z., et al. 2024b, Research in Astronomy and Astrophysics, 24, 115003

¹⁷ Department of Astronomy & Center for Galaxy Evolution Research, Yonsei University, Seoul 03722, Republic of Korea

¹⁸ Instituto de Ciencias Exactas y Naturales (ICEN), Universidad Arturo Prat, Chile

¹⁹ Astrophysics Research Institute, Liverpool John Moores University, 146 Brownlow Hill, Liverpool L3 5RF, UK

²⁰ Univ Lyon, Univ Claude Bernard Lyon 1, CNRS, IP2I Lyon/IN2P3, UMR 5822, F-69622, Villeurbanne, France

²¹ Center for Interdisciplinary Exploration and Research in Astrophysics (CIERA), Northwestern University, 1800 Sherman Ave., Evanston, IL 60201, USA

²² Department of Astronomy, Stockholm University, 10691 Stockholm, Sweden

²³ Henan Academy of Sciences, Zhengzhou 450046, Henan, China

¹ Institut für Physik, Humboldt-Universität zu Berlin, Newtonstr. 15, 12489 Berlin, Germany

² Deutsches Elektronen-Synchrotron, 15735 Zeuthen, Germany

³ Leibniz-Institut für Astrophysik Potsdam (AIP), An der Sternwarte 16, 14482 Potsdam, Germany

⁴ European Southern Observatory, Alonso de Córdova 3107, Casilla 19, Santiago, Chile

⁵ DIRAC Institute, Department of Astronomy, University of Washington, 3910 15th Avenue NE, Seattle, WA 98195, USA

⁶ School of Physics, Trinity College Dublin, The University of Dublin, Dublin 2, Ireland

⁷ IPAC, California Institute of Technology, 1200 E. California Blvd, Pasadena, CA 91125, USA

⁸ Graduate Institute of Astronomy, National Central University, 300 Jhongda Road, 32001 Jhongli, Taiwan

⁹ Department of Physics, Lancaster University, Lancs LA1 4YB, UK

¹⁰ Institute of Space Sciences (ICE, CSIC), Campus UAB, Carrer de Can Magrans, s/n, E-08193 Barcelona, Spain

¹¹ Institut d'Estudis Espacials de Catalunya (IEEC), Edifici RDIT, Campus UPC, 08860 Castelldefels (Barcelona), Spain

¹² Oskar Klein Centre, Department of Physics, Stockholm University, Albanova University Center, SE 106 91 Stockholm, Sweden

¹³ Division of Physics, Mathematics and Astronomy, California Institute of Technology, Pasadena, CA 91125, USA

¹⁴ Astronomical Observatory, University of Warsaw, Al. Ujazdowskie 4, 00-478 Warszawa, Poland

¹⁵ Caltech Optical Observatories, California Institute of Technology, Pasadena, CA 91125

¹⁶ Cardiff Hub for Astrophysics Research and Technology, School of Physics & Astronomy, Cardiff University, Queens Buildings, The Parade, Cardiff, CF24 3AA, UK

Appendix A: K-correction spectral templates

Section 3.2 details the method used to compute K-corrections for our augmented samples. Table A.1 lists the `sncosmo` template models employed in this process.

Table A.1: `sncosmo` templates for K-corrections

SN type	<code>sncosmo</code> template
SN Ia and subtypes	salt2
SN Ib, Ib-pec and Ib _n	v19-iptf13bvn-corr
SN Ib/c	v19-iptf13bvn-corr
SN Ic and Icn	v19-2013ge-corr
SN Ic-BL	v19-2012ap-corr
SN II and II-pec	v19-2016bkv-corr
SN II _b and II _b -pec	v19-2016gkg-corr
SN IIL	s11-2004hx
SN IIP	snana-2007iz
SN IIn	v19-2011ht-corr

Notes. The relevant references for each spectral template are found at sncosmo.readthedocs.io/en/stable/source-list.html.

Appendix B: Example augmented light curves

Section 3 details the procedure used to generate the augmented light curves used in our training and test samples. Figures B.1 and B.2 present examples of augmented SN Ia and SN II light curves, respectively. For comparison, each panel includes a real light curve at a similar redshift, illustrating that the augmented data exhibit realistic brightness evolution and scatter consistent with real observations. The augmented light curves shown were drawn from the training sample, generated using the augmentation parameters: `z_scale` = 0, `cadence_scale` = 100, `subsampling_rate` = 0.9.

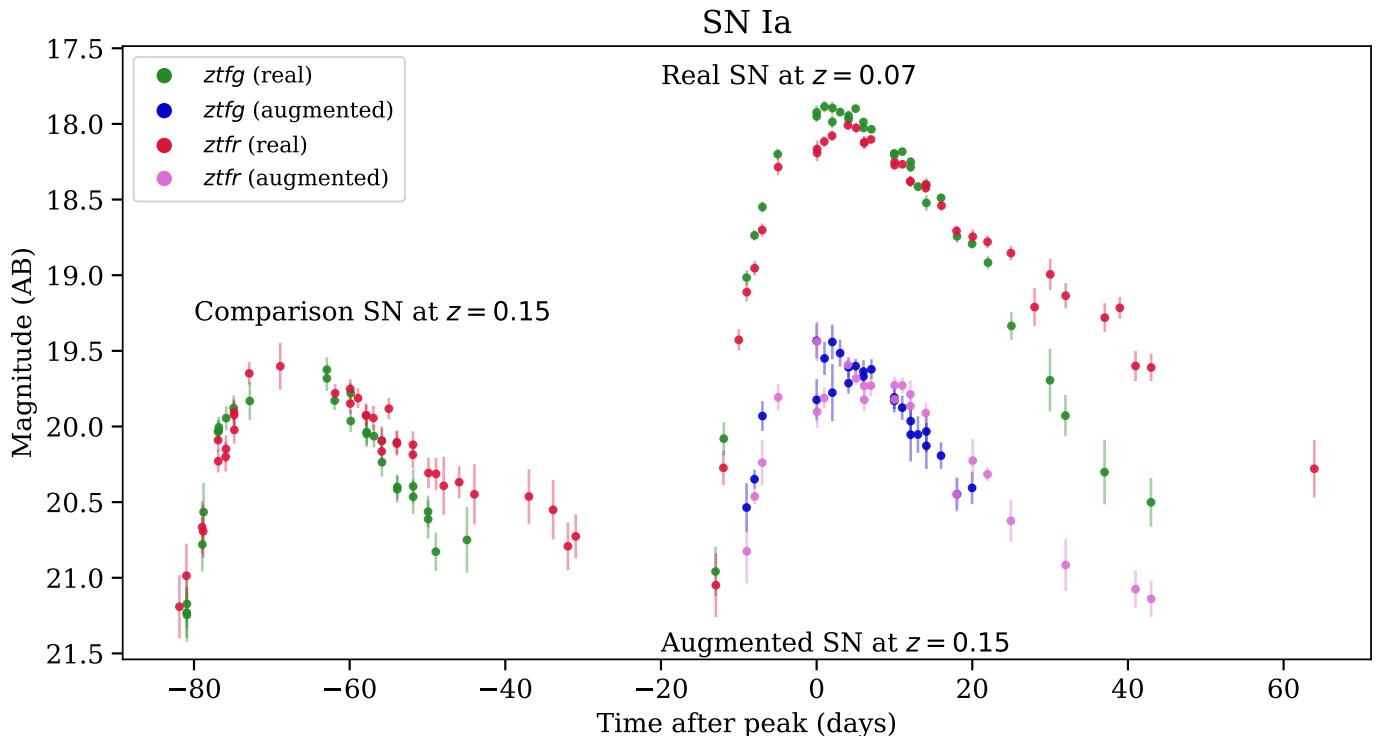


Fig. B.1: Comparison of a real, bright SN Ia (SN 2021vts at $z = 0.072$), its augmented counterpart at higher redshift ($z = 0.147$), and a real SN Ia at a similar redshift (SN 2021kfy at $z = 0.15$). Data points are shown in the *g*-band (green for real, pink for augmented) and *r*-band (red for real, blue for augmented); the *i*-band is omitted for clarity. Time is shown relative to the peak of SN 2021vts, with an offset applied to SN 2021kfy to aid comparison.

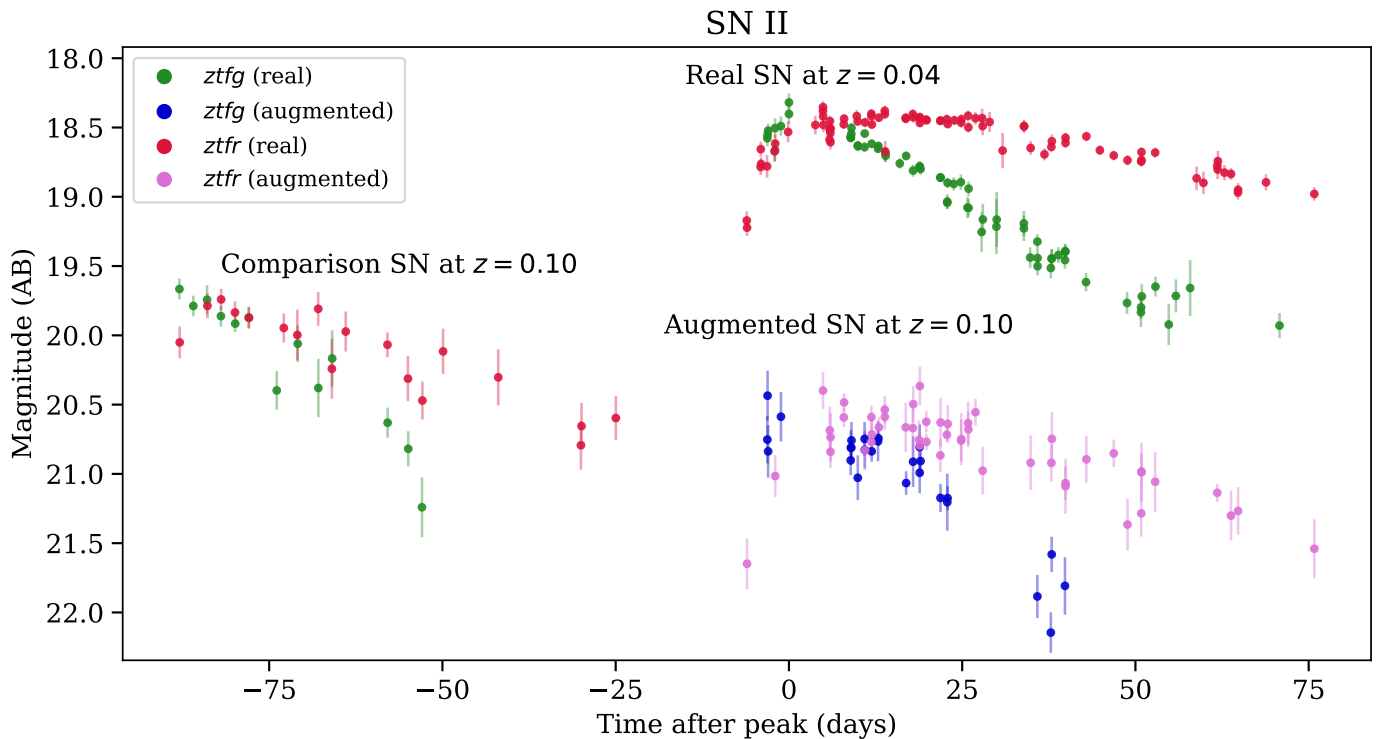


Fig. B.2: Comparison of a real, bright SN II (SN 2022jnh at $z = 0.038$), its augmented counterpart at higher redshift ($z = 0.095$), and a real SN II at a similar redshift (SN 2020whv at $z = 0.097$). Data points are shown in the g -band (green for real, pink for augmented) and r -band (red for real, blue for augmented); the i -band is omitted for clarity. Time is shown relative to the peak of SN 2022jnh, with an offset applied to SN 2020whv to aid comparison. Note that, unlike SNe Ia, SNe II have more diverse peak luminosities, so the augmented and comparison light curves peak at different magnitudes.

Appendix C: Augmentation parameter optimisation: cadence_scale and subsampling_rate

Section 5.1 outlines the augmentation parameters we tested to optimise classifier performance. While class scaling had the most significant impact, we also observed a weaker dependence on the `cadence_scale` and `subsampling_rate` parameters. As shown in Figs. C.1 and C.2, SN Ia recall was highest when no data points were removed, whereas SN Other recall improved with more aggressive subsampling.

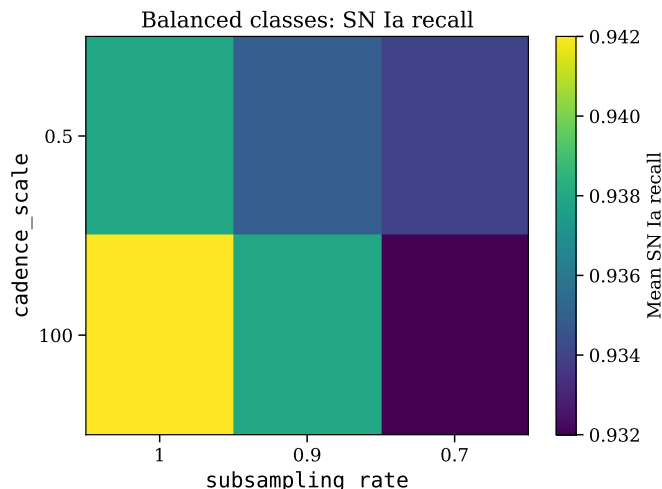


Fig. C.1: Mean SN Ia recall, averaged over multiple iterations of the FaintZTF and FaintZTF+Noise test sets (with balanced class scaling), as a function of the augmentation parameters `cadence_scale` and `subsampling_rate`. The highest recall occurs when no data points are removed, corresponding to `cadence_scale` = 100 and `subsampling_rate` = 1.

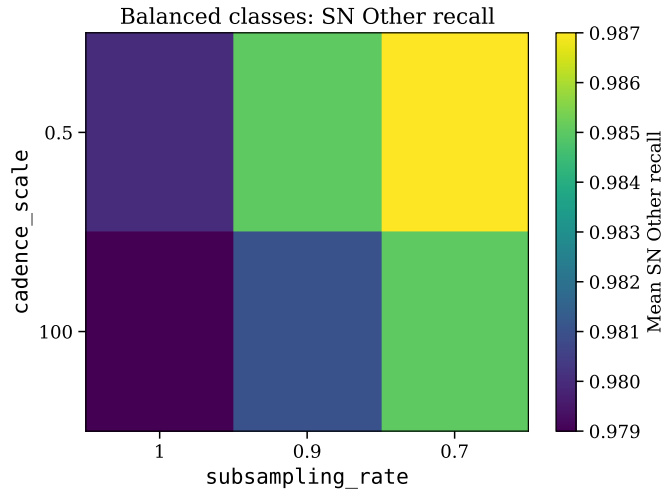


Fig. C.2: Mean SN Other recall, averaged over multiple iterations of the FaintZTF and FaintZTF+Noise test sets (with balanced class scaling), as a function of the augmentation parameters `cadence_scale` and `subsampling_rate`. Performance shows a slight preference for more aggressive data removal, with optimal values around `cadence_scale` = 0.5 and `subsampling_rate` = 0.7.

Appendix D: Confusion matrices for the BrightZTF and FaintZTF training and test samples

We discuss in Sect. 5.2 how SN Ia recall improves with augmentation in the training sample, resulting in better classification of fainter, noisier light curves. Figure D.1 shows the confusion matrices, normalised by true class totals (i.e., by row), to display the recall across different augmentation combinations of BrightZTF and FaintZTF.

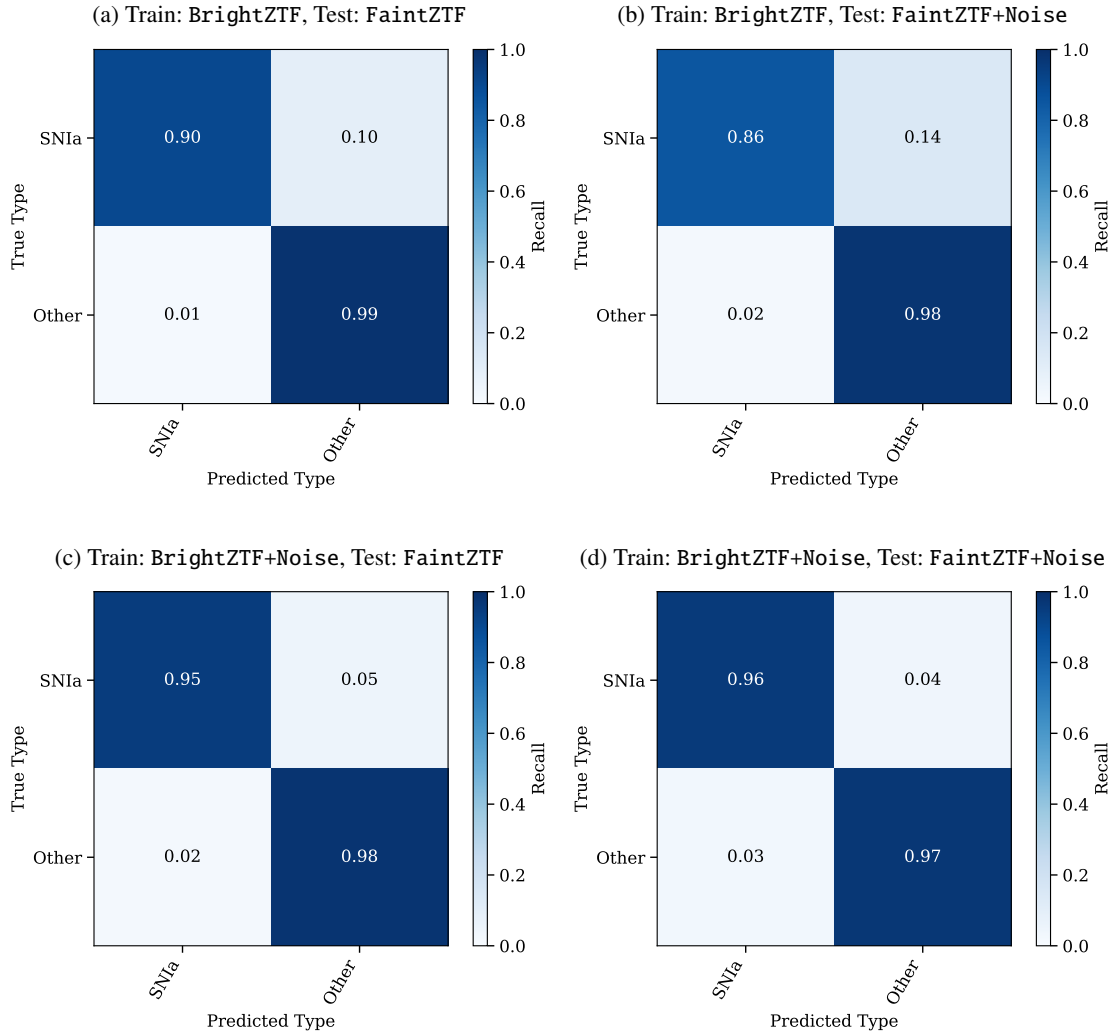


Fig. D.1: Confusion matrices for our selected model configuration (bolded in Table 3), normalised by true class totals (i.e., by row) to display the recall across different augmentation combinations of BrightZTF and FaintZTF. The four plots correspond to: (a) training and testing on unaugmented data, (b) training on unaugmented data and testing on augmented data, (c) training on augmented data and testing on unaugmented data, and (d) training and testing on augmented data. The results demonstrate that noise augmentation in the training set improves classification performance on fainter, noisier test samples.

Appendix E: The NoiZTF survey: classification results

In Sect. 5.6, we presented the NoiZTF survey, a spectroscopic follow-up program designed to select interesting candidates and evaluate the photometric classifications produced by our classifier. Table E.1 summarises the results from this classification survey.

Figure E.1 shows a late-phase spectrum of SN 2024qef, taken on 2 October 2024 by the ePESSTO+ collaboration as part of a follow-up program, approximately 80 days after the first detection. The data was reduced¹⁰, and spectral template fitting was performed using the python wrapper `pysnid`¹¹ of the Supernova Identification code (SNID; Blondin & Tonry 2007)¹². The two best-matching templates correspond to a peculiar Type Ib and a broad-lined Type Ic, both at a redshift of $z \sim 0.28$. Combining this redshift with the photometric data (peak apparent magnitude $r_{ZTF} \sim 19.3$) results in a peak absolute magnitude of $M < -21$, which is consistent with an SLSN-I interpretation. If this interpretation is correct, it suggests that the photometric classification was more informative than the early-phase spectroscopy, which produced only a blue, featureless spectrum. This highlights the potential of photometric classifiers to provide meaningful classifications in cases where spectroscopy is inconclusive – particularly during the early phases, when certain transients are intrinsically featureless.

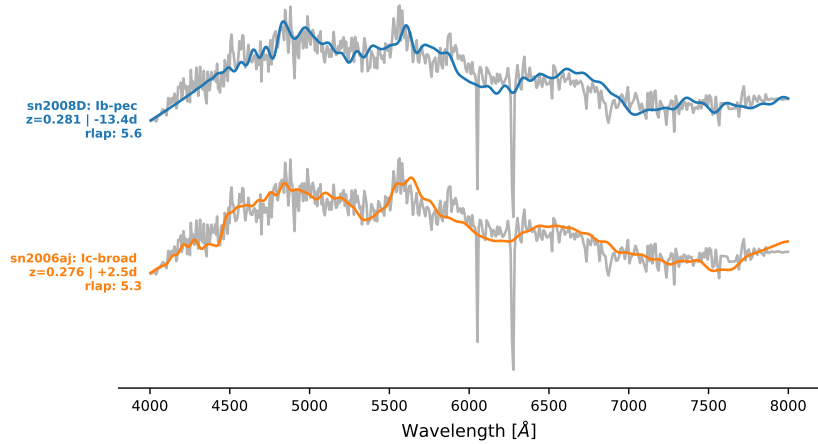


Fig. E.1: A late-phase spectrum of SN 2024qef, taken on 2 October 2024 by the ePESSTO+ collaboration as part of a follow-up program, approximately 80 days after the first detection. The two best-matching spectral templates correspond to a peculiar Type Ib (blue) and a broad-lined Type Ic (orange), both at a redshift of $z \sim 0.28$.

¹⁰ github.com/svalenti/pessto

¹¹ github.com/MickaelRigault/pysnid

¹² people.lam.fr/blondin.stephane/software/snid/

Table E.1: NoiZTF classification survey results.

ZTF name	IAU name	Predicted class	True class	No. of detections	Reference
ZTF24aaooxcd ¹	SN 2024jfh	SN II	SN II	33	Gonzalez-Gaitan et al. (2024)
ZTF24aarqqug	SN 2024lhf	SN Ia	SN Ia	27	Gonzalez-Banuelos et al. (2024a)
ZTF24aardmeg	SN 2024lcm	SN Ia	SN Ia	8	Gonzalez-Gaitan et al. (2024)
ZTF24aapzmaf	SN 2024kng	SN Ia	SN Ia	13	Gonzalez-Gaitan et al. (2024)
ZTF24aaowjlw	SN 2024jwx	SLSN	SLSN	33	Gonzalez-Banuelos et al. (2024b)
ZTF24aarqrkn ²	SN 2024kzu	SLSN	SN Ia	24	Duarte et al. (2024a)
ZTF24aarkrxi	SN 2024lgz	SN II	SN II	29	Gonzalez-Gaitan et al. (2024)
ZTF24aaumhmm	SN 2024nzi	SN Ia	SN Ia	7	Gonzalez-Gaitan et al. (2024)
ZTF24aauerna	SN 2024nzf	SN Ia	SN Ia	17	Duarte et al. (2024b)
ZTF24aaumgko	SN 2024nzg	SN Ia	SN Ia	5	Duarte et al. (2024b)
ZTF24aashinc	SN 2024ltj	SN Ia	SN Ia	13	Duarte et al. (2024a)
ZTF24aaseunp	SN 2024lrp	SN Ia	SN Ia	7	Duarte et al. (2024a)
ZTF24aaxhvb ³	SN 2024qef	SLSN	SN	29	Moore et al. (2024)
ZTF24aaysowl	SN 2024rmj	SLSN	SLSN	9	Shitrit et al. (2024a)
ZTF24abbjtjc	SN 2024ser	SN Ia	SN Ia	13	Shitrit et al. (2024a)
ZTF24aasteui ⁴	TDE 2024mvz	SLSN	TDE	16	Shitrit et al. (2024a)
ZTF24aatsmxc	SN 2024nbv	SN II	SN II	24	Mohsen et al. (2024)
ZTF24abcrsy ²	SN 2024sbx	SLSN	SN II	9	Dgany et al. (2024)
ZTF24abavoif ⁵	SN 2024seh	SN Ia	SN II	15	Mehta et al. (2024)
ZTF24abcnnlb	SN 2024snk	SN Ia	SN Ia	6	Shitrit et al. (2024b)
ZTF24abbsuhu ⁶	SN 2024sjw	SN Ia	SN Ib/c	7	Mohsen et al. (2024)
ZTF24abbggnw	SN 2024nrw	SLSN	SLSN	7	Moore et al. (2024)
ZTF24abayoiy	SN 2024sjd	SN Ia	SN Ia	5	Shitrit et al. (2024a)
ZTF24abeiasc ⁷	SN 2024uhx	SLSN	SN	13	Ramirez et al. (2024b)
ZTF24abamahv ⁸	AT 2024syj	SLSN	-	12	Dimitriadis et al. (2024)
ZTF24aaxqoeo	SN 2024pll	SN II	SN II	7	Ramirez et al. (2024a)
ZTF24abojqpw	SN 2024zgv	SN Ia	SN Ia	8	Pessi et al. (2024b)
ZTF24aboiwjo ²	SN 2024zjt	SLSN	SN Ia	7	Hu et al. (2024)
ZTF24abiyona	SN 2024uki	SN II	SN II	15	Ramirez et al. (2024b)
ZTF24abrddqo	SN 2024aaqc	SN Ia	SN Ia	6	Pessi et al. (2024a)
ZTF24abpdzvm ^{9,10}	SN 2024zsw	SN II	SN II	19	Gagliano (2024)
ZTF24abpvane	SN 2024zwm	SN Ia	SN Ia	8	Tsalapatas et al. (2024)
ZTF24abrkfol ¹⁰	SN 2024abbi	SN Ia	SN Ia	6	Sollerman et al. (2024b)
ZTF24abtbalq	SN 2024abop	SN Ia	SN II	9	Townsend et al. (2024a)
ZTF24abrfiya	SN 2024aasm	SN Ia	SN II	9	Townsend et al. (2024b)
ZTF24abrfhyl ¹⁰	SN 2024aaqs	SN II	SN II	8	Blagorodnova et al. (2024)
ZTF24abqbyxd ¹⁰	SN 2024zzf	SN II	SN Ib/c	9	Fremling et al. (2024)
ZTF24abpiwwi ^{9,11}	SN 2024aaks	SLSN	SLSN-IIIn	40	Angus (2024)
ZTF24abtcetf ¹⁰	SN 2024abnt	SN Ia	SN Ia	7	Sollerman et al. (2024a)
ZTF24abubygj ¹⁰	SN 2024acon	SN Ia	SN Ia	6	Covarrubias et al. (2024)

¹ SN 2024jfh was initially photometrically classified as an SN Ia with $p > 0.7$ at 23 detections, which changed to an SN II with $p = 0.65$ at 33 detections.

² These objects were likely photometrically classified as SLSNe due to an erroneous high photometric redshift ($z > 0.4$) from a catalogue crossmatch.

³ SN 2024qef was classified as an SN with a blue featureless spectrum. Follow-up spectra from ePESSTO+ taken at later phases have good matches to Ib-pec or Ic-BL at $z \sim 0.28$. This would mean a peak absolute magnitude of $M < -21$ mag, suggesting the true type could be an SLSN-I.

⁴ Given that the TDE was not available to the classifier, a prediction of SLSN is the most likely outcome.

⁵ SN 2024seh was initially classified as SN by ePESSTO+, and then further classified as SN II by another group.

⁶ SN 2024sjw was classified as an SN Ib.

⁷ SN 2024uhx was classified as an SN with a blue featureless spectrum.

⁸ AT 2024syj was observed, but the spectrum was too noisy for a conclusive classification. However, its light curve duration of over 100 days is consistent with an SLSN.

⁹ SN 2024zsw was further classified as an SN IIb by a Young Supernova Experiment group.

¹⁰ Not classified by ePESSTO+, but by a ZTF groups reporting to TNS.

¹¹ Classified by the SCAT group as an SN IIIn. However, the peak absolute magnitude of this object is $M < -21$ mag, suggesting it is an SLSN-IIIn.

Notes. The number of detections refers to those available at the time of photometric classification, not at the time of spectroscopic classification. Classifications and spectra are publicly available at: wis-tns.org.